JCTC Journal of Chemical Theory and Computation

Article

Cite This: J. Chem. Theory Comput. 2020, 16, 18−34

pubs.acs.org/JCTC

Quantum Dynamics with the Quantum Trajectory-Guided Adaptable Gaussian Bases

Matthew Dutra, Sachith Wickramasinghe, and Sophya Garashchuk*

Department of Chemistry and Biochemistry, University of South Carolina, Columbia, South Carolina 29208, United States

ABSTRACT: The computational cost of describing a general quantum system fully coupled by anharmonic interactions scales exponentially with the system size. Thus, an efficient basis representation of wave functions is essential, and when it comes to the large-amplitude motion of high-dimensional systems, the dynamic bases of Gaussian functions are often employed. The time dependence of such bases is determined from the variational principle or from classical dynamics; the former is challenging in implementation due to singular matrices, while the latter may not cover the configuration space relevant to quantum dynamics. Here we describe a method using Quantum Trajectory-guided Adaptable Gaussian (QTAG) bases "tuned"—including the basis position, phase, and width—to the wave function evolution, thanks to the continuity of the probability density in the course of the quantum trajectory dynamics. Thus, an efficient basis in configuration space is generated, bypassing the variational equations on the parameters of the Gaussians. We also propose a time propagator with basis transformation by projections which lends efficiency and stability to the QTAG dynamics, as demonstrated on standard tests and the ammonia inversion model.

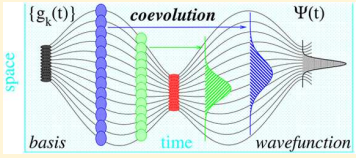

1. INTRODUCTION

The importance of the quantum-mechanical (**QM**) effects associated with nuclei is gaining recognition in chemistry and physics, as researchers manipulate matter, light, electric, and magnetic fields at the atomistic level to develop advanced materials and molecular structures with desired properties. A few recent examples of experimentally observed nuclear quantum effects (**NQE**s) in molecular systems include the dependence of optoelectronic properties of the poly(3-hexylthiophene)/phenyl-C61-butyric acid methyl ester heterojunction on the hydrogen/deuterium substitution of the polymer,[1] isotope effects on the proton conductance in low-dimensional boron nitrides and silicon-based structures[2] and on crystallinity of poly(3-hexylthiophene),[3] polymerization of benzene under pressure,[4] and the spin response of aluminum tris(8-hydroxyquinoline).[5] Generally, the NQEs are most prominent for light nuclei at low temperatures, when the typical energy of a process is comparable to the separation between the vibrational energy levels of chemical bonds.

The quantum behavior of the nuclei is governed by the time-dependent Schrödinger equation (**TDSE**) with a (possibly time-dependent) potential,

$$\hat{H}\psi(x, t) = \imath\hbar\frac{\partial}{\partial t}\psi(x, t), \quad \hat{H} = \hat{T} + \hat{V} \tag{1}$$

For a particle of mass m (described here for simplicity in one dimension), the Hamiltonian $\hat{H}$ is a sum of the kinetic and potential energy operators, $\hat{T}$ and $\hat{V}$,

$$\hat{T} := -\frac{\hbar^2}{2m}\nabla^2, \quad \hat{V} := V(x) \tag{2}$$

The potential V will be referred to as the "classical" potential. The time dependence of V will be omitted, but it is not a limitation of the formalism. The gradient symbol will be used throughout to indicate differentiation with respect to x: $\nabla f := \partial f(x, t)/\partial x$.

Computational efforts of describing a general (i.e., anharmonic) fully coupled quantum system scale exponentially with the system size due to the inherent structure of quantum mechanics (as argued, for example, in ref 6). Therefore, an efficient basis representation of wave functions is essential for the studies of high-dimensional molecular systems. There is a number of established approaches to solve eq 1 for the nuclei by explicit wave function time propagation, such as the split-operator/fast Fourier transform (SOFT), the Chebyshev propagator expansion, or the iterative Hamiltonian diagonalization.[7−11] Beyond low-dimensional systems, however, there is no standard approach of generating a wave function representation which would remain accurate and practical in the course of dynamics involving large-amplitude motion.

The conventional direct-product finite basis or discrete variable representations, even with efficient truncation and contraction schemes, are impractical, if not unfeasible, for exact full-dimensional descriptions of systems of more than five atoms (nine spatial dimensions).[12] Therefore, general approaches of generating correlated representations tailored to the evolving wave function and the desired "outputs" of a calculation—which may include observables, correlation functions, and spectra of acceptable accuracy—are highly sought after. Despite the generally exponential scaling of the TDSE solutions with the system size, modest-size bases adapted to the wavepacket time evolution may be adequate for obtaining, for example, low-lying energy eigenstates or a medium resolution spectrum.

Received: August 22, 2019
Published: December 4, 2019

DOI: 10.1021/acs.jctc.9b00844
J. Chem. Theory Comput. 2020, 16, 18−34

Over the years numerous efforts have gone into the development of exact QM dynamics utilizing the time-dependent bases, as well as approximate and semiclassical dynamics methods, which are not reviewed here for brevity. The most accomplished exact QM dynamics approach, balancing computational cost and accuracy, is the multi-configuration time-dependent Hartree method (**MCTDH**), which employs contraction of a general basis to single (or a few) particle functions according to the time-dependent variational principle.[13−15] The Gaussian-based version of the MCTDH—the variational multiconfiguration Gaussian approach[16−18]—is most similar to the dynamics method presented here, which employs the quantum-trajectory guided adaptable Gaussian (**QTAG**) bases. Other relevant Gaussian-based approaches are mentioned in the upcoming sections. In general, Gaussian functions are heavily used in quantum dynamics, because a Gaussian wave function (or a Gaussian multiplied by a polynomial) solves the TDSE for a locally parabolic potential. Moreover, the harmonic oscillator model is the foundation for the normal-mode analysis of molecular vibrations, and a time-dependent Gaussian wavepacket is frequently used to describe a spatially localized nearly-classical particle. Mathematical properties of Gaussian functions (localization in coordinate and momentum spaces, analytic integrals, Gaussian quadrature, etc.) are also appealing from the practical point of view. The ever-growing efficiency of the electronic structure calculations and advances in the potential energy surface (**PES**) construction (such as the product representation[19,20] and fitting/interpolation methods[21,22]) makes evaluation of the potential matrix elements over a Gaussian basis practical and enables on-the-fly wavepacket dynamics.[23,24]

In the remainder of this paper, we describe an exact quantum dynamics approach utilizing flexible Gaussian bases, specified by adjustable "width" (spatial localization), position, and linear phase parameters, whose time dependence is guided by quantum trajectory dynamics, rather than by the variational principle. The formal connection between the variational principle and quantum trajectory dynamics is given in Section 2. Details of implementation are given in Section 3, followed by several numerical examples and discussion in Section 4. Section 5 gives a summary and an outlook.

2. ADAPTABLE GAUSSIAN BASES GUIDED BY THE QUANTUM TRAJECTORIES

To streamline notations, the formalism is presented for a one-dimensional system using atomic units, i.e., $\hbar = 1$. Its generalization to many dimensions is given in Appendix D.

2.1. Wave Function Representation in the Time-Dependent Basis. In order to solve the TDSE 1 in coordinate space, a wave function $\psi(x, t)$ is represented in a generally nonorthogonal basis of N_b functions, $\{g_j\}$, where $j \in [1, N_b]$. At time t, the wave function is expressed as a superposition of these functions,

$$\psi(x, t) = \sum_{j=1}^{N_b} c_j(t) g_j(x, t) \tag{3}$$

with c_j denoting the expansion coefficients. The latter can be arranged as a vector $\vec{c}$ with elements $c_1, c_2, ..., c_{Nb}$. The jth basis function depends on time through N_p parameters enumerated by the index $\alpha \in [1, N_p]$. We will consider the Gaussian basis functions (**GBFs**),

$$g_j := g_j(x; \vec{\lambda}_j(t)) = \left(\frac{a_j}{\pi}\right)^{1/4} \exp\left(-\frac{a_j}{2}(x - q_j)^2 + \imath p_j(x - q_j) + \imath s_j\right) \tag{4}$$

each specified by a list of parameters, arranged as components of the vector $\vec{\lambda}_j$,

$$\vec{\lambda}_j(t) = (a_j, q_j, p_j, s_j)^T \tag{5}$$

For simplicity, let us assume that N_b does not change in time and that N_p is the same for all basis functions. The time derivative of such a basis function is equal to

$$\frac{\partial g_j}{\partial t} = \sum_{\alpha=1}^{N_p} \dot{\lambda}_{j\alpha} \partial g_{j\alpha} \tag{6}$$

$$\dot{\lambda}_{j\alpha} := \frac{\mathrm{d}\lambda_{j\alpha}}{dt}, \qquad \partial g_{j\alpha} := \frac{\partial g_j}{\partial \lambda_{j\alpha}} \tag{7}$$

The time dependence of the expansion coefficients is obtained by substituting eqs 3 and 6 into the TDSE 1 and minimizing the error functional ϵ,

$$\epsilon = \int_{x\in\mathbf{R}} |\hat{H}\psi - \imath\partial\psi/\partial t|^2 \, \mathrm{d}x, \tag{8}$$

with respect to $\mathrm{d}c_j^*/\mathrm{d}t$, which yields the matrix equation

$$\imath\mathbf{S}\frac{\mathrm{d}\vec{c}}{\mathrm{d}t} = (\mathbf{H} - \imath\mathbf{D})\vec{c} \tag{9}$$

Minimization with respect to $\mathrm{d}c_j/\mathrm{d}t$ gives a redundant system of equations complex-conjugate to eq 9. Above and throughout, **S** is the overlap matrix,

$$S_{jl} = \langle g_j | g_l \rangle \tag{10}$$

and **H** is the Hamiltonian matrix,

$$H_{jl} = \langle g_j | \hat{H} | g_l \rangle \tag{11}$$

The nonhermitian matrix **D** accounts for the time dependence of the basis functions,

$$D_{jl} = \sum_{\alpha=1}^{N_p} \langle g_j | \dot{\lambda}_{l\alpha} \partial g_{l\alpha} \rangle \tag{12}$$

The initial value for $\vec{c}$ at $t = 0$ is given by the expansion of $\psi(x, 0)$ in a basis,

$$\vec{c}(0) = \mathbf{S}^{-1} \langle \vec{g}(x) | \psi(x, 0) \rangle \tag{13}$$

with the elements of $\vec{g}(x)$ being the GBFs.

The choice of the time dependence of the basis functions, i.e., of the parameters $\vec{\lambda}_j(t)$, $j \in [1, N_b]$ (eq 5), determines the accuracy and conservation properties of the dynamics. As shown, for example, in ref 25, the normalization of the wave function evolved according to eq 9 is conserved regardless of the basis completeness or time dependence. The total energy,

$$E = \langle \psi(x, t) | \hat{H} | \psi(x, t) \rangle \tag{14}$$

is conserved in three cases: (i) for *any* time-independent (stationary) basis; (ii) for a time-dependent basis with parameters determined variationally; and (iii) for a basis with arbitrary time-dependence, which is *complete* in a sense of

DOI: 10.1021/acs.jctc.9b00844
J. Chem. Theory Comput. 2020, 16, 18−34

representing $\psi(x, t)$. Thus, the norm conservation can be used to monitor the numerical accuracy of propagation, and the energy conservation indicates the basis completeness.

Out of the variational GBF methods the Gaussian MCTDH, or the frozen-width Gaussian MCTDH, are the most developed.[14,26−28] It has been noted, however, that the variational equations on the Gaussian parameters are ill-conditioned, and the solutions may become physically nonintuitive with time and are challenging to converge numerically.[16,29] Overall, the combination of Gaussian functions representing the spectator modes with the variationally determined contraction of conventional bases (which is the original MCTDH) describing the active modes has been found more robust and enabled challenging high-dimensional applications.[17,18,30]

As an alternative to variational GBFs, a number of the quantum dynamics methods, including nonadiabatic dynamics, based on nonvariational GBFs have been developed.[31−35] The GBF parameters typically come from the positions and momenta of classical or Ehrenfest-type trajectories. Of particular relevance here is dynamics based on the coupled coherent states (**CCS**),[36−38] which follow classical trajectories sampling the phase space. The advantage of the methods with predefined time-dependence of the basis functions is that the variational eq 9 for the expansion coefficients alone is much easier to implement numerically compared to the full set of variational equations. The disadvantage is the usual concern for quasi- and semiclassical approaches: certain regions of space relevant to the exact quantum evolution may be inaccessible to the classical trajectories, as is known to happen in tunneling processes. The fully variational GBFs interact and "exchange" energy through the coupled equations of motion, allowing some of the trajectories to reach the classically forbidden regions.[26,39] To address this issue, we therefore consider GBFs inspired by the *quantum* trajectory (**QT**) formulation of the TDSE,[40−42] summarized in Appendix A. The most relevant features of the QT dynamics are: (**i**) the QT momentum is defined by the wave function phase evaluated at the QT position q_t, $p = \nabla \arg(\psi(x, t))|_{x=q_t}$; (**ii**) the QTs interact via the quantum potential of eq 60, formally generating *all* quantum effects including tunneling and interference; and (**iii**) the QT dynamics satisfies the continuity of the probability density $\rho = |\psi(x, t)|^2$,

$$\frac{\mathrm{d}\rho}{\mathrm{d}t} = -\frac{\nabla p}{m}\rho \tag{15}$$

Equation 15 implies that an ensemble of the QT positions can be interpreted as an "optimal" time-dependent grid whose points follow the flow of the probability density in time.

2.2. Time Dependence of the GBF Parameters. Now let us turn to the variation of the error functional with respect to the GBF parameters (loosely following the notations of ref 30). For simplicity, for each GBF the variational procedure here includes the first three parameters from eq 5,

$$\lambda_{j1} = a_j, \quad \lambda_{j2} = q_j, \quad \lambda_{j3} = p_j, \quad j \in [1, N_b] \tag{16}$$

arranged into a single vector $\vec{\Lambda}$,

$$\vec{\Lambda} = (a_1, q_1, p_1, a_2, q_2, p_2, ..., a_{N_b}, q_{N_b}, p_{N_b})^T \tag{17}$$

Each GBF is centered at the *trajectory position* q_j; p_j specifies the *linear*-in-x phase. Note that, generally, $p_j \neq m\dot{q}_j$. All parameters, including the GBF width, a_j, are *real* functions of time. Going back to the definition of the GBF, the last element in $\vec{\lambda}_j$ of eq 5 is an *x-independent* phase, s_j, which can be combined with c_j. Therefore, its time dependence cannot be derived from the variational principle. The role of s_j is to reduce the temporal oscillations of c_j, which improves stability of the time propagation as shown, for example, in ref 39. In the QTAG dynamics s_j naturally emerges from the equations of motion as the action function along a trajectory.

Given $\mathrm{d}\vec{c}/\mathrm{d}t$ of eq 9, minimization of eq 8 with respect to $\dot{\lambda}_{j\alpha}$ for $j \in [1, N_b]$ leads to the following equations of motion:

$$\mathbf{B}\frac{\mathrm{d}}{\mathrm{d}t}\vec{\Lambda} = \vec{Y} \tag{18}$$

The size of the matrix $\mathbf{B}$ and vector $\vec{Y}$ is equal to the total number of the GBF parameters included in the variational procedure; in this presentation, this size is $3 \times N_b$. The elements of the matrix $\mathbf{B}$ and vector $\vec{Y}$ are

$$B_{j\alpha,l\beta} = \mathcal{R}(\rho_{jl}(S_{jl}^{(\alpha\beta)} - [\mathbf{S}^{(\alpha 0)}\mathbf{S}^{-1}\mathbf{S}^{(0\beta)}]_{jl})) \tag{19}$$

$$Y_{j\alpha} = \mathcal{I}\left(\sum_l \rho_{jl}(H_{jl}^{(\alpha 0)} - [\mathbf{S}^{(\alpha 0)}\mathbf{S}^{-1}\mathbf{H}]_{jl})\right) \tag{20}$$

where

$$\rho_{jl} := c_j^* c_l \tag{21}$$

The use of $\mathcal{R}$ and $\mathcal{I}$ seen in eqs 19 and 20 and throughout the remainder of this work refer to the real and imaginary components, respectively, of the relevant arguments. The remaining matrices are the counterparts to $\mathbf{S}$ and $\mathbf{H}$ with the parameter derivatives $\partial g_{j\alpha}$ replacing some of the GBFs:

$$H_{jl}^{(\alpha 0)} := \langle \partial g_{j\alpha} | \hat{H} g_l \rangle \tag{22}$$

$$S_{jl}^{(\alpha 0)} := \langle \partial g_{j\alpha} | g_l \rangle, \quad S_{jl}^{(\alpha\beta)} := \langle \partial g_{j\alpha} | \partial g_{l\beta} \rangle \tag{23}$$

To emphasize the physical meaning of the solutions to eq 18, we will rewrite $\mathbf{B}$ and $\vec{Y}$ using the resolution of identity in the basis, i.e., the operator $\mathbb{I}$,

$$\mathbb{I} := |\vec{g}\rangle \mathbf{S}^{-1} \langle \vec{g}| \tag{24}$$

and the unit matrix $\mathbf{I}$:

$$B_{j\alpha,l\beta} = \mathcal{R}(\rho_{jl}[\langle \partial\vec{g}_\alpha \otimes |\mathbf{I} - \mathbb{I}| \otimes \partial\vec{g}_\beta \rangle]_{jl}) \tag{25}$$

$$Y_{j\alpha} = \mathcal{I}\left(\sum_l \rho_{jl}[\langle \partial\vec{g}_\alpha \otimes |\mathbf{I} - \mathbb{I}| \otimes \hat{H}\vec{g} \rangle]_{jl}\right) \tag{26}$$

The formal solution to the variational eq 18 depends on the structure of the operator $\mathbf{I} - \mathbb{I}$ which defines the subspace of functions complementary to that covered by the given basis. Thus, the system of eqs 18 is numerically ill-defined/singular when the GBF is large/complete in a sense of representing $\psi(x, t)$ or, in other words, when the error functional 8 is insensitive to the GBF variations. The problems and some ways to mitigate them are reviewed in ref 30. We will, however, focus on another solution to eq 18, when *each* g_l approaches the exact solution to the TDSE,

$$\imath \sum_\beta \partial g_{l\beta}\dot{\lambda}_{l\beta} = \hat{H} g_l \tag{27}$$

DOI: 10.1021/acs.jctc.9b00844
J. Chem. Theory Comput. 2020, 16, 18−34

i.e., in the regime when g_l is localized on the scale of the anharmonicity of $V(x)$ and of the wave function amplitude. The time dependence of such functions has a physical interpretation in terms of the quantum trajectory dynamics, as argued below.

Consider a normalized GBF ($a_t > 0$),

$$g(x, t) = \left(\frac{a_t}{\pi}\right)^{1/4} \exp\left(-\frac{a_t}{2}(x - q_t)^2 + \imath\mathcal{S}(q_t) + \imath\mathcal{S}'(q_t)(x - q_t) + \frac{\imath\mathcal{S}''(q_t)}{2}(x - q_t)^2\right) \tag{28}$$

which approximately solves the TDSE for the classical potential $V(x)$. The phase of $g(x, t)$ is the quadratic expansion of the wave function phase,

$$\mathcal{S}(x, t) := \arg(\psi(x, t)) \tag{29}$$

$$\mathcal{S}(x, t) \approx \mathcal{S}(q_t) + \mathcal{S}'(q_t)(x - q_t) + \frac{\mathcal{S}''(q_t)}{2}(x - q_t)^2 \tag{30}$$

The GBF parameters in eq 28 are real functions of time indicated by the subscript. Substitution of eq 28 into

$$g^{-1}\left(\hat{H}g - \imath\frac{\partial g}{\partial t}\right) = 0 \tag{31}$$

gives a complex equation whose imaginary part yields the following equations of motion for q_t and a_t,

$$\dot{q}_t = \frac{\mathcal{S}'(q_t)}{m}, \quad \dot{a}_t = -\frac{2\mathcal{S}''(q_t)}{m}a_t \tag{32}$$

As shown in Appendix B, in the Lagrangian frame-of-reference ($\mathrm{d}/\mathrm{d}t = \partial/\partial t + \dot{q}_t\nabla$), for *any* $V(x)$, the real part of eq 31 can be recast as

$$\frac{\mathrm{d}\mathcal{S}}{\mathrm{d}t} = \frac{(\nabla\mathcal{S})^2}{2m} - V(x) - U_g(x) \tag{33}$$

where the potential-like term U_g,

$$U_g(x) := -\frac{a_t^2(x - q_t)^2}{2m} + \frac{a_t}{2m} \tag{34}$$

is consistent with the quantum potential (eq 60) associated with a Gaussian wave function of the form of eq 28. Thus, identifying the phase gradient with the QT momentum, $\nabla\mathcal{S}|_{x=q_t} = p_t$ (eq 63), eq 33 is equivalent to the quantum Hamilton–Jacobi eq 66. The ensuing trajectory equations of motion,

$$\dot{q}_t = \frac{p_t}{m}, \quad \dot{p}_t = -\nabla(U + V)|_{x=q_t} \tag{35}$$

define the quantum (or Bohmian) trajectory $\{q_t, p_t\}$. Therefore, we argue that the "locally optimal" GBF parameters are consistent with the QT dynamics.

The time-dependent GBF discussed above is related to the well-known thawed Gaussian wavepacket (TGWP).[43] The TGWP, which is an exact solution to the TDSE for a locally parabolic $V(x)$, is a Gaussian of the form given by eq 28, except that its phase is *quadratic* in x, effectively making its width parameter complex. The evolution equations for the TGWP parameters form a closed set involving the Hessian of $V(x)$.[44] The TGWP center moves classically; its overall phase $\mathcal{S}_t$, however, has a contribution due to the quantum potential through the last RHS term of the evolution equation,

$$\frac{\mathrm{d}\mathcal{S}(q_t)}{\mathrm{d}t} = \frac{p_t^2}{2m} - V(q_t) - \frac{a_t}{2m} \tag{36}$$

At the Gaussian center, q_t, the quantum potential (U_g of eq 34) generates zero quantum force and is reduced to the time-dependent constant $U_g(q_t) = a_t/(2m)$. Even though the TGWP describes exact QM dynamics in a parabolic potential, use of multiple thawed Gaussians as basis functions has been found to be impractical due to their complex "width" parameters; depending on the Hessian, a_t may become negative, resulting in a non-normalizable GBF. Moreover, the integration of Gaussians with quadratic phase requires careful sign tracking. Consequently, most exact or semiclassical Gaussian-based dynamics methods utilize frozen Gaussians with a time-independent real width parameter.[45,46] In QTAG dynamics we employ Gaussian basis functions of real width whose evolution depends on the wave function rather than on the Hessian of $V(x)$ directly. The GBF phase is restricted to be a *linear* function of x; thus, the GBF overlaps and other matrix elements are straightforwardly computed. The linear phase and time dependent width are both optional; bases consisting of real frozen GBFs guided by the quantum trajectories provide a more numerically robust (at the expense of a larger basis size) option.[47]

To summarize, the equations of motion for the parameters of the adaptable GBFs of eq 4 are

$$\dot{q}_j = \frac{p_j}{m}, \quad \dot{a}_j = -\frac{2a_j}{m}\nabla p_j, \quad \dot{s}_j = \frac{p_j^2}{2m} - V(q_j) - U(q_j) \tag{37}$$

and the multidimensional generalization is given in Appendix D. The right-hand sides in eqs 37 are given by the log-derivative of $\psi(x, t)$, z_j,

$$z_j := \left.\frac{\nabla\psi(x, t)}{\psi(x, t)}\right|_{x=q_t} \tag{38}$$

and its gradient. The real and imaginary components of z_j define the classical and nonclassical momenta p_j and r_j, respectively,

$$p_j := \nabla\mathcal{S}(q_j) = \mathcal{I}(z_j) \quad r_j := \nabla\ln(\mathcal{A}(q_j)) = \mathcal{R}(z_j) \tag{39}$$

Note that while ∇p_j defines the evolution of a_j and ∇r_j is needed to evolve the phase s_j (through eq 62 defining U_j), only p_j is required to evolve the main parameter, which is the GBF center q_j. (Recall that s_j, introduced to reduce oscillations of the expansion coefficients, is altogether redundant and can be set to zero or taken as the classical action function.) Moreover, use of an approximate z_j *does not* introduce approximations into the formalism, although the resulting basis is not guaranteed to be as efficient as the one tracking the probability density flow along the exact QTs. In fact, when describing dynamics with interference, the exact QTs are known to be numerically unstable; however, since a superposition of GBFs captures such behavior, one simply needs to get the GBFs to the "right place at the right time" to maintain an accurate description of the system. Therefore, in practice we use a modified z_j (employing a low-order polynomial fitting or

DOI: 10.1021/acs.jctc.9b00844
J. Chem. Theory Comput. 2020, 16, 18−34

Gaussian convolution to act as low-pass filters) to evolve the GBF parameters according to eqs 37, generating guiding trajectories that are smoother and more stable then the exact QTs (Section 3.2).

3. NUMERICAL IMPLEMENTATION

In this section we describe the time propagation algorithm and procedures essential to the implementation of the QTAG dynamics.

3.1. Propagation Employing Basis Orthogonalization/Basis Transformation. The time evolution of the expansion coefficients, governed by eq 9, involves analytic time derivatives of the GBF parameters and the nonhermitian matrix in the right-hand side. To solve the coupled eqs 9 and 37 we have adopted the following time propagation scheme, which combines wave function time evolution in the energy eigenstate representation with basis transformations. A time-dependent wave function represented in a static nonorthogonal basis (eqs 3 and 4) is constructed from solutions to the generalized eigenvalue problem:

$$\mathbf{HZ} = \mathbf{SZ}\mathcal{E} \tag{40}$$

The elements of the Hamiltonian ($\mathbf{H}$) and overlap ($\mathbf{S}$) matrices—both hermitian—are given by eqs 11 and 10, respectively. The diagonal matrix $\mathcal{E}$ contains the energy eigenvalues, $\mathcal{E}_{jj} = \varepsilon_j$, while the columns of the matrix $\mathbf{Z}$ give the Hamiltonian eigenvectors in a basis $\vec{g}$. The eigenvectors satisfy the following relationships:

$$\mathbf{Z}^{\dagger}\mathbf{SZ} = \mathbf{I}, \quad \mathbf{ZZ}^{\dagger} = \mathbf{S}^{-1} \tag{41}$$

For the sake of derivation, let us divide the total propagation time into equal time intervals of length τ. The use of variable time intervals does not change this propagation algorithm. To describe the GBF time dependence, we will use the superscript (k) to label the basis (and any object evaluated in that basis) corresponding to the kth time interval. For example, the GBF of eq 4 at $t = k\tau$ is

$$g_j^{(k)} \equiv g_j(x; \vec{\lambda}_j(k\tau)) \tag{42}$$

and so forth. The superscript (0) will denote the initial basis and related objects at time $t = 0$. The time evolution over the kth time interval, i.e., $t = [\tau(k-1),\tau k]$, is comprised of two conceptual operations: (i) propagation of a wave function in the energy eigenstates defined in the "old" basis $\vec{g}^{(k-1)}$ and (ii) an update of the GBF positions and, possibly, other parameters in $\vec{\Lambda}$ according to the local behavior of the wave function $\psi(x, k\tau)$.

(i) For a wave function $\psi(x, t)$ represented in the basis $\vec{g}^{(k)}$ according to eq 3, the expansion coefficients $\vec{c}^{(k)}(t)$ are related to the projection vector $\vec{b}^{(k)}(t)$ as

$$\vec{c}^{(k)}(t) = (\mathbf{S}^{(k)})^{-1}\vec{b}^{(k)}(t),$$
$$\text{where } \vec{b}^{(k)}(t) = \langle \vec{g}^{(k)}(x)|\psi(x, t)\rangle \tag{43}$$

Starting with $t = 0$, i.e., $k = 0$, the updated wave function $\psi(x, \tau)$ in the *old* basis $\vec{g}^{(0)}$ is given by the expansion coefficients $\vec{c}^{(0)}(\tau)$,

$$\vec{c}^{(0)}(\tau) = \mathbf{K}_{\tau}^{(0)}\vec{b}^{(0)}(0) \tag{44}$$

where $\mathbf{K}_{\tau}^{(0)}$ denotes the propagator matrix and its subscript indicates the time increment τ,

$$\mathbf{K}_{\tau}^{(0)} = \mathbf{Z}^{(0)} \exp(-\imath\mathcal{E}^{(0)}\tau)(\mathbf{Z}^{(0)})^{\dagger} \tag{45}$$

The exponential term in eq 45 is a diagonal matrix with nonzero elements $\exp(-i\varepsilon_j\tau)$ for $j = [1, N_b]$. The superscripts T and $\dagger$ throughout indicate the transpose and conjugate transpose, respectively.

(ii) Given $\psi(x, \tau)$, the new momenta p_j are computed according to eq 39 at $q_j^{(0)}$, and the GBF positions are updated (in the simplest way) as $q_j^{(1)} = q_j^{(0)} + p_j\tau/m$. These GBFs form the *new* basis $\vec{g}^{(1)}$. To complete the first time interval, i.e., evolution from $t = 0$ to $t = \tau$, the basis change is incorporated via the transformation matrix $\mathbf{T}^{(1,0)}$ with elements

$$T_{jl}^{(1,0)} = \langle g_j^{(1)}|g_l^{(0)}\rangle \tag{46}$$

The expansion coefficients $\vec{c}^{(1)}(\tau)$ in the new basis, minimizing the basis representation error of $\psi(x, \tau)$, are

$$\vec{c}^{(1)}(\tau) = (\mathbf{S}^{(1)})^{-1}\mathbf{T}^{(1,0)}\vec{c}^{(0)}(\tau) \tag{47}$$

where $\vec{c}^{(0)}(\tau)$ are given by eq 44. After propagation over K time intervals the wave function at $t = K\tau$ becomes

$$\psi(x, K\tau) = (\vec{g}^{(K-1)})^{T}\left(\prod_{k=2}^{K}\mathbf{K}_{\tau}^{(k-1)}\mathbf{T}^{(k-1,k-2)}\right)\mathbf{K}_{\tau}^{(0)}\vec{b}^{(0)}(0) \tag{48}$$

The flow of the propagation algorithm is sketched in the right-hand side loop in Figure 1. Additional details are given in Appendix C.

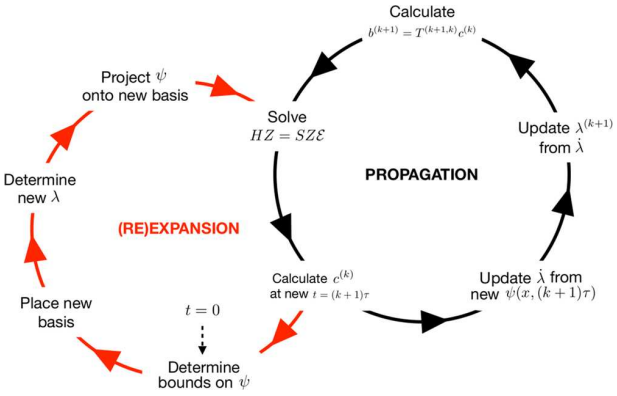

Figure 1. Time evolution algorithm: (left) steps of the expansion, or reexpansion, of a wave function in a basis; (right) time propagation with basis orthogonalization and transformations (BOT). A simulation begins at the $t = 0$ label, completes the left (red) loop, and propagates along the right (black) loop until a reexpansion criterion is met—at which point the (re)expansion branch is again taken—or the simulation completes. See text for the reexpansion criteria.

The primary advantage to the diagonalization step (i) is that use of the energy eigenstates enables much larger time steps compared to straightforward integration of eq 9 via Runge–Kutta-type methods as has been done previously.[47] Another advantage is that the wave function can be reconstructed at *any* moment of time within the intervals τ and used to compute desired output, e.g., correlation functions, or assess basis completeness on a time scale shorter than τ. To achieve the latter and adjust τ accordingly one can also monitor the wave

DOI: 10.1021/acs.jctc.9b00844
J. Chem. Theory Comput. 2020, 16, 18−34

function energy and norm conservation upon the basis transformation at the end of each propagation cycle.

Conservation of the wave function normalization, $N = \langle\psi|\psi\rangle$, and total energy, $E = \langle\psi|\hat{H}|\psi\rangle$, depends on the basis completeness at the transformation step. Over each time interval τ, i.e., for each k, the wave function norm and energy are obviously conserved since the GBFs are static. Employing eqs 47 and 46, N and E represented within the bases $\vec{g}^{(0)}$ and $\vec{g}^{(1)}$ after a single time step are

$$N^{(1)} = (\vec{c}^{(1)})^{\dagger}(\mathbf{S}^{(1)})^{-1}\vec{c}^{(1)} = (\vec{c}^{(0)})^{\dagger}\langle\vec{g}^{(0)} \otimes | \mathbb{I}^{(1)}| \otimes \vec{g}^{(0)}\rangle\vec{c}^{(0)} \approx (\vec{c}^{(0)})^{\dagger}\mathbf{S}^{(0)}\vec{c}^{(0)} = N^{(0)} \tag{49}$$

$$E^{(1)} = (\vec{c}^{(0)})^{\dagger}\langle\vec{g}^{(0)} \otimes \mathbb{I}^{(1)}\hat{H}\mathbb{I}^{(1)}| \otimes \vec{g}^{(0)}\rangle\vec{c}^{(0)} \approx (\vec{c}^{(0)})^{\dagger}\mathbf{H}^{(0)}\vec{c}^{(0)} = E^{(0)} \tag{50}$$

The operator $\mathbb{I}^{(1)}$ denotes the resolution of identity in the basis $\vec{g}^{(1)}$ defined by eq 24. The norm, energy, and expansion coefficients in eqs 49 and 50 are evaluated at $t = \tau$. The approximate equality in both eqs 49 and 50 becomes exact in the complete basis limit, i.e., as $\mathbb{I}^{(1)} \to \mathbf{I}$, where $\mathbf{I}$ is the unit matrix of the size $N_b^{(1)}$. By extrapolating the relationships above to all time slices, it is evident that both the energy and the wave function norm are conserved to the extent that the chosen basis yields an accurate representation of the true wave function. The error associated with the basis incompleteness depends on the closeness of $\mathbb{I}^{(k+1)}$ to the unit matrix $\mathbf{I}$ of the same size, specifically, as $\langle\mathbb{I}^{(k+1)} - \mathbf{I}\rangle$ for the wave function norm, and as $\langle(\mathbb{I}^{(k+1)} - \mathbf{I})^2\rangle$ for its energy.

Finally, at the basis transformation step (**ii**) the wave function can be reexpanded in a new basis (Section 3.3) that has been changed *discontinuously*, including all the GBF parameters and the basis size as sketched in the left-hand-side loop in Figure 1.

3.2. Updating the GBF Basis. The main challenge inherent to the GBF evolution as defined by eqs 37 is the numerical stability of the trajectories upon which the basis functions are centered. Conceptually, these QTs are tied to the shape of the wave function: the density of Bohmian paths is high where the wave function density is high and correspondingly lower where the wave function density is lower. In the former case, the close proximity of the paths can cause the basis overlap matrix $\mathbf{S}$ to become singular. Another problematic scenario arises when considering the nodes of the wave function: the QTs passing close to the nodal regions will have large, rapidly changing instantaneous momenta leading to propagation errors and breakdown. At the same time, if one considers quantum motion which is largely confined within a limited region of space, a static basis is likely to provide the best practical representation despite significant interference exhibited by the wave function.

In both cases, to preserve the essence of the QTs—updating the GBFs according to the probability flow—while addressing the instances of numerical instability, we define the trajectory momenta at q_t using $\psi(x, t)$ and its derivatives over the region of space centered at q_t, rather than simply using their values at q_t. There are several options for this modification. The momenta can be defined from a wave function (eq 3) or convoluted with a Gaussian as in ref 47. Alternatively, they can be computed at the GBF centers and fitted to a low-order polynomial function or convoluted with the Gaussian kernel. The output of either procedure is then used to advance the GBF center and other parameters in time. The convolution acts as a low-pass filter of the Bohmian momenta, specified by the parameter β, and controls the propagation stability. The order of the polynomial is the counterpart to β when fitting (which can be performed on the entire space or on the trajectory centered subspaces) is used.

For a Gaussian convolution, the log-derivative z_j (eq 38) is computed from $\psi(x, t)$ defined in a basis, and the result is averaged with a window function $\omega_{\beta jl}$,

$$\omega_{\beta jl} := \exp(-\beta(q_l - q_j)^2) \tag{51}$$

The resulting modified classical and nonclassical momenta, $\tilde{p}_j$ and $\tilde{r}_j$ are

$$\tilde{p}_j = \frac{\sum_l \mathcal{I}(z_l)\omega_{\beta jl}}{\sum_l \omega_{\beta jl}}, \qquad \tilde{r}_j = \frac{\sum_l \mathcal{R}(z_l)\omega_{\beta jl}}{\sum_l \omega_{\beta jl}} \tag{52}$$

The trajectory is updated as $q_j(t + \tau) = q_j(t) + \tilde{p}_j\tau/m$. The quantum potential in eq 37 is determined by using $\tilde{r}$ in eq 62. We estimate the remaining term (∇r_j), the linear GBF phase (p_j), and the time increment of a_j (dependent on ∇p_j) from the global least squares fit (**LSF**) to $\nabla(\ln \psi)$. The linear-in-x fit is exact for a Gaussian wave function. A few other fitting schemes have been considered, e.g., defining the momentum from a convoluted wave function and performing the linear fit localized by a Gaussian window function of eq 51. In both cases, for a Gaussian wave function characterized by the width γ, the relative error in the fitting coefficients is $\sim(\gamma/\beta + 1)^{-1}$. In our experience so far, these schemes did not offer numerical advantages or superior accuracy for the dynamics, but this result may be application-dependent.

3.3. Wave Function Reexpansion. As mentioned previously, the basis description of the wave function—including all parameters listed in eq 5 and their total number N_p—can be instantaneously modified during any basis transformation step (ii) of Section 3.1. These reexpansion processes are used to extend the accuracy and efficiency of the basis representation to longer simulation times and can be initiated whenever the current basis becomes an inadequate representation of the total wave function. Conceptually, these situations can occur because the trajectories upon which the GBFs travel are not exactly quantum (see eq 52, for example) but merely QT-inspired. In addition to this, the basis can also become incomplete if the wave function becomes very disperse relative to the basis width parameter—which is itself somewhat width-limited by the harmonic approximation to the potential—and a larger total number of GBFs is needed to fill in the "holes".

There are three main questions that accompany the wave function reexpansion procedure, and the manner in which each is addressed can vary with the system that is being studied. These questions are, in the order they are encountered in a simulation: (i) *when* to initiate reexpansion, (ii) *how* to place the new basis functions, and (iii) *what* criteria are used to determine when the wave function is sufficiently represented in the new basis (i.e., when to stop the reexpansion process).

The simplest solution to (i) is to perform reexpansions regularly at predefined time intervals and to test sensitivity of the results to the frequency of reexpansions. However, because this approach is inherently insensitive to the underlying wave function dynamics, time may be wasted performing needless reexpansions if the simulation is already stable. Alternatively,

DOI: 10.1021/acs.jctc.9b00844
J. Chem. Theory Comput. 2020, 16, 18−34

Table 1. System, Initial Wavefunction, and Basis Parameters[a]

system			wavepacket			basis	
potential	m	γ	X_0	P_0	N_b	a/γ	ρ_c
harmonic oscillator: $V = kx^2/2$							
$k = 1$	1.0	0.8	1.0	1.0	15	8	10^{-12}
anharmonic bath: $V = \sum_{i=1,3} D(\exp(-\zeta(x_i - x_e)) - 1)^2 + \kappa \sum_j \sum_{i<j} (x_i - x_e)(x_j - x_e)$							
$D = 0.1743$, $x_e = 1.4$, $\zeta = 1.0435$, $\kappa = 0.1$	925.0	9.16	1.3, 1.4, 1.4	0.0	7, 107, 843	7	10^{-5}
Wu−Batista model: $V = b_4 x_1^4 + b_2 x_1^2 + \sum_{j=2}^{N} (x_j^2/2 + \kappa x_j x_{j-1})$							
$b_4 = 0.0461459$, $b_2 = -0.5$, $\kappa = 0.2$	1.0	0.5	−2.5, 0.0	0.0	$17 \times 2^{N-1}$	4, 2.3	10^{-5}
NH_3 double well: $V = b_0 + b_2 x^2 + b_4 x^4$							
$b_0 = 0.008566$, $b_2 = -0.03139$, $b_4 = 0.02875$	5508.0	24.8	0.7	0.0	19	8	10^{-10}
NH_3 coupled mode: $V_c = \kappa xy + ky^2/2$							
$b_2 = -0.03139$, $b_4 = 0.02875$, $\kappa = 0.1893$, $k = 0.007181$	3671.0	12.0	0.0	0.0	11	7.5	10^{-10}

[a]All quantities are listed in the atomic units. In the anharmonic bath model the three values of X_0 refer to the wavepacket centers in dimensions 1, 2, and 3, respectively; the three values of N_b refer to one-, two-, and three-dimensional calculations.

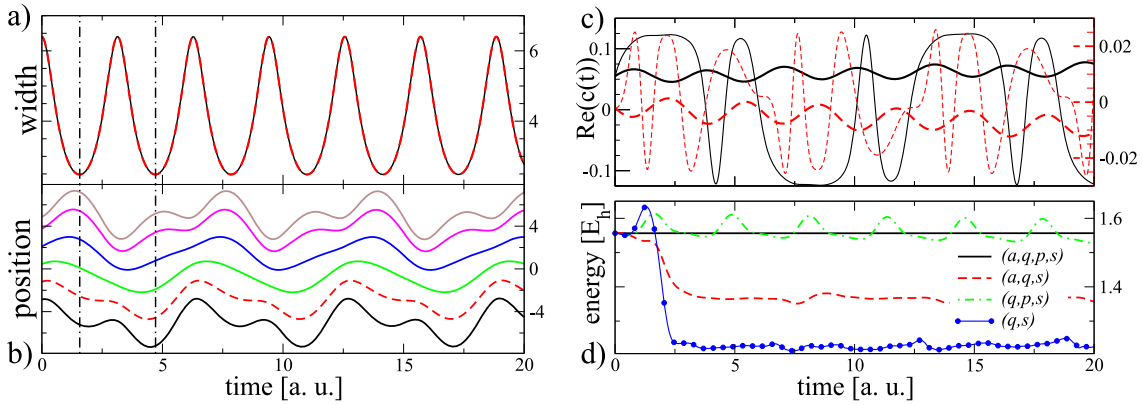

Figure 2. QTAG dynamics of the harmonic oscillator: GBF (a) widths, $\{a_j\}$, and (b) positions, $\{q_j\}$, are given in atomic units; times of the largest wave function spreading are marked with dashed vertical lines over the first period of motion in each panel. (c) The real parts of the expansion coefficients for two selected GBFs with the overall phase factor s_j included (black solid line, vertical scale on left) and excluded (red dashed line, vertical scale on right) from the GBF definition; (d) total energy for several combinations of the adjustable GBF parameters specified in the legend.

the wave function energy throughout the dynamics may be monitored, as deviations indicate basis incompleteness. The total energy is an easily computed global criterion, although a more sensitive marker for system stability, which we find highly useful in NH_3 tunneling (Section 4.4), is to monitor the energy change, dE/dq_j, due to displacements of the fringe trajectories. This parametric derivative, which is a force acting on the GBF center,

$$\frac{dE}{dq_j} = \frac{dE/dt}{dq_j/dt} \tag{53}$$

can be computed numerically throughout the simulation (we use the third-order backward finite difference method). Conceptually, when this value is large, the total energy is sensitive to the movement of the jth GBF; we interpret this to mean that the regions near the edge of the GBF-populated space (specifically, near the jth GBF) are becoming important to the description of the system, and additional GBFs may be needed to ensure a sufficient density of GBFs in the relevant area.

(ii) Several reexpansion strategies have been proposed in the literature, such as Matching Pursuit[48] and Basis Expansion Leaping,[49] based on the reduction of the residual error in the new basis from the detailed analysis of the target wave function or its residual. In another two methods, namely, the short-time trajectories[50] and the moving grid boundary method,[51] the basis is adjusted according to the anticipated motion of the wave function. The first three schemes have been developed for the GBF dynamics, while the latter adjusts the conventional equidistant grid according to the Bohmian momentum at the grid edges. In this work, we propose a simpler approach for high-dimensionality systems: new GBF positions, $\{q_j\}$, are generated through some quasirandom sampling method and are accepted/rejected depending on the probability density at a point, which should exceed a predetermined cutoff density, ρ_c,

$$|\psi(q_j, t)|^2 > \rho_c \tag{54}$$

This approach does not involve optimization of the GBF parameters and can incorporate importance sampling techniques[52] or recently developed quasi-regular grids.[53] The width parameters $\{a_j\}$ can be taken equal to the original GBF value or be commensurate with the density of $\{q_j\}$, provided the local harmonic approximation to V remains accurate. The GBF momenta $\{p_j\}$, if used, are defined from the wave function as described in Section 3.2. The initial phases $\{s_j\}$ are set to zero. This random sampling of the wave function has been shown to exhibit good scaling in ref 54 for time-independent bound problems; it is applied in this work to the anharmonic bath model of Section 4.2. In the future we intend to combine information about existing GBF positions, probability density,

DOI: 10.1021/acs.jctc.9b00844
J. Chem. Theory Comput. 2020, 16, 18−34

and the wave function flux analysis, i.e., the Bohmian momenta, and quasi-regular grids to generate new bases without loss of the wave function norm due to poor old/new basis overlaps, an issue of concern in high-dimensional applications.

(iii) The sampling is finished when the norm and the kinetic energy of the reexpanded wave function match the old values within certain tolerances. Checking for norm conservation alone is insufficient, and comparing the total energies of the two wave functions is more computationally expensive due to the potential matrix evaluation. Numerical comparison of the local wave function gradients can also be used as a check for completeness; this criterion is likely to be more accurate but also more computationally expensive.

4. APPLICATIONS AND DISCUSSION

To illustrate the QTAG method, we consider wave function dynamics in several model potentials. The initial wave function is taken as a Gaussian wavepacket in each case,

$$\psi(x, 0) = \left(\frac{2\gamma}{\pi}\right)^{1/4} \exp(-\gamma(x - X_0)^2 + \imath P_0(x - X_0)) \tag{55}$$

or, in multiple dimensions, as a product of such wavepackets. Parameters of the potentials, initial wave functions, and bases are summarized in Table 1.

4.1. Dynamics with Fully Adaptable Gaussian Bases.

First, we consider dynamics of the harmonic oscillator. For the conditions specified in Table 1, the initially displaced noncoherent Gaussian wavepacket exhibits both oscillatory and breathing motions. The wavepacket is represented by 15 GBFs, equally spaced within the range of $|\psi(x, 0)|^2$ exceeding the threshold value $\rho_c = 10^{-12}$. The GBF parameters are evolved according to eqs 37 with the time step of $\tau = 0.01$ au. The adaptable GBFs have up to four parameters $\{a_j, q_j, p_j, s_j\}$ for $j \in [1, N_b]$, representing the width, center position, linear phase, and overall phase, respectively. The time dependence of the GBF widths and positions is shown in Figure 2. For a Gaussian wavepacket characterized by the quadratic-in-x phase, the momentum is linear in x and its gradient is constant. Thus, the GBF widths $\{a_j\}$, shown in Figure 2a, exhibit the same time dependence for all functions; in this example $\{a_j\}$ changes by a factor of 4. The GBF centers $\{q_j\}$ (Figure 2b) change their spacing following the expansion and contraction of the probability density and are updated according to the momenta determined by the fit of z_j (eq 38) to linear functions—a procedure which is exact for a Gaussian wavepacket. Note that, for fully converged simulations, this means the $\{q_j\}$ are identical to the quantum trajectories *regardless* of whether $\{a_j\}$ and $\{p_j\}$ are kept constant or adapted to the evolving wave function. The overall GBF phases $\{s_j\}$ do not affect the basis completeness; their role is to reduce the oscillatory behavior of the expansion coefficients $\{c_j\}$, which enables larger time steps during propagation. This effect is seen in Figure 2c, which displays the real part of c_j for two selected trajectories.

The effect of the "QT-optimized" GBF parameters on the basis completeness is assessed from the system energy, shown in Figure 2d for four combinations of the time-dependent GBF parameters. All four calculations employ identical bases of 15 GBFs at $t = 0$ and are shown for up to 20 au of time (about three oscillation periods). The most accurate energy conservation is achieved by employing GBFs with time-dependent $\{a_j, q_j, p_j, s_j\}$ (black curve). Inclusion of the linear-in-x phase $p_j(x - q_j)$ in the GBFs improves the representation of the high-energy components of $\psi(x, t)$, which is especially useful in describing the overall translational motion. Its impact is seen by comparing calculations performed with (black curve) and without (red curve) this phase; in the latter case the energy quickly drops and never recovers, signaling inadequate basis representation. Similar behavior is seen when the GBF width is subsequently frozen (blue curve). Interestingly, the calculation with adjustable width and without the linear GBF phase yields oscillatory total energy (green curve). This behavior is explained by the "holes" between the GBFs developing as the QTs reach their maximal spread. To better illustrate this behavior, we have examined the effect of the basis parameters on the basis completeness through the energy time dependence and its correlation with the nearest-neighbor GBF overlap, shown in Figure 3. The energy conservation (Figure 3a) is worst at the maximal separation of the GBF centers, which correlates with the drop in the GBF overlap shown in Figure 3. GBFs that are wider (magenta dashed line) or more densely spaced (green dashed line) improve the energy conservation, while adaptable a_j (black line, same time dependence as in Figure 2a) compensates for the trajectory spreading altogether.

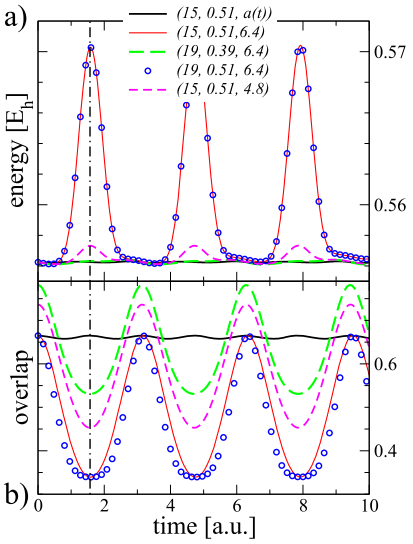

Figure 3. QTAG dynamics of the harmonic oscillator: (a) total energy and (b) the nearest neighbor GBF overlap as functions of time for the bases specified in the legend. The number of basis functions N_b, the initial GBF spacing $\Delta q = q_{j+1} - q_j$, and width a_j are listed as $(N_b, \Delta q, a_j)$. The GBF widths are frozen except for the curves labeled "$a(t)$" in the legend (thin black lines): for these results the time dependence of $a(t)$ is given by eq 37 for $a(0) = 6.4a_0^{-2}$.

The effect of various combinations of time-dependent parameters on the simulation stability is evaluated via the conservation of the wave function normalization for propagations implemented using both the Runge−Kutta-type integration of eq 9 and the basis orthogonalization/transformation (BOT) algorithm of Section 3.1. The standard deviation of the wave function normalization over time $t = [0, 10]$ au for the propagation time step of $\tau = 0.001$ au is listed in Table 2, using the system parameters given in Table 1. In seven out of eight cases the BOT propagation is more accurate; the

DOI: 10.1021/acs.jctc.9b00844
J. Chem. Theory Comput. 2020, 16, 18−34

Table 2. Standard Deviation in the Wavefunction Normalization during the Dynamics Performed by Integration of Equation 9 and Using the Basis Orthogonalization/Transformation Procedure[a]

$\vec{\lambda}(t)$	integration	time slicing
(a, q, p, s)	1.13×10^{-4}	9.09×10^{-7}
(a, q, s)	9.74×10^{-4}	6.73×10^{-4}
(q, s)	5.19×10^{-6}	2.74×10^{-4}
(q, s)	3.24×10^{-4}	5.406×10^{-4}
(a, q, p)	4.23×10^{-3}	7.07×10^{-7}
(a, q)	3.67×10^{-3}	1.62×10^{-4}
(q, p)	4.32×10^{-3}	2.73×10^{-4}
(q)	4.18×10^{-3}	2.501×10^{-4}

[a]The final propagation time is 10 a.u. with a time step 0.001 a.u. for all calculations of the harmonic oscillator system specified in Table 1. The time-dependent GBF parameters, $\vec{\lambda}(t)$, are listed in the first column.

largest improvement (by a factor of over 100) is seen for the fully converged basis with time-dependent $\{a_j, q_j, p_j\}$. We also note that inclusion of $\{s_j\}$ improves the conventional integration scheme (the standard deviation is reduced by a factor of 5), rather than the BOT scheme. The reason is that, within the latter, the overall phase effect is included analytically over each time slice.

The basis completeness for the four combinations of time-dependent GBF parameters, namely, $\{a_j, q_j, p_j\}$, $\{q_j, p_j\}$, $\{a_j, q_j\}$, and $\{q_j\}$, has been tested for the Morse oscillator mimicking the H_2 stretch (the parameters are the same as those of the first coordinate of the "anharmonic bath" entry in Table 1). For the system initially displaced from equilibrium by 0.1 a_0, the best energy and norm conservation during the dynamics with seven basis functions was obtained for real GBFs with adaptable width ($\{a_j, q_j\}$). This result is consistent with our general observation that, while the GBFs with QT-consistent width and linear phase yield more efficient wave function representation, (i) for realistic potentials the variations in $\{a_j\}$ will be limited by the accuracy of the local harmonic approximation invoked to compute the potential energy matrix elements, and that, overall, (ii) propagation with real frozen Gaussians is numerically more robust, due to the real nature of their overlap and Hamiltonian matrices.

4.2. Model Anharmonic Bath. The scalability of the QTAG method in higher-dimensional systems is investigated using systems of coupled and uncoupled Morse oscillators in one, two, and three dimensions. The oscillator parameters are listed in Table 1 under the "anharmonic bath" entry. The initial wave function is a Gaussian of appropriate dimensionality centered at the minimum of the well with the exception of the first dimension, which is displaced by 0.1 a_0 toward the repulsive wall. The initial basis functions are distributed uniformly according to the appropriately scaled quasirandom Sobol sequence. An accept−reject criterion based on the wave function density then determines whether a basis placement is accepted; the parameter N_b is thus determined on-the-fly by stopping placement when a normalization condition is met. The initial displacement X_0 is taken to be exclusively in one dimension for all systems presented; coupling between the dimensions (in the coupled scenarios) is of the form $V(x_i, x_j) = \kappa \sum_j \sum_{i<j} (x_i - x_e)(x_j - x_e)$, where $\kappa = 0.1\ E_h a_0^{-2}$. The simulation durations of $t = 1300$ au capture about two periods of motion. The bases are of frozen width and fully real, with initial sizes $N_b = 7$, 107, and 843 for one, two, and three dimensions, respectively. Ultimately, no reexpansions were necessary in any of the systems.

Simulation accuracy can be tracked through the energy eigenvalues; the time-averaged values of the first four levels in each system are presented in Table 3. For the uncoupled cases, the agreement between the QTAG and analytic values extends to two or three decimal places in each entry. In the scenarios with coupled degrees of freedom, we also track the energy as it flows between dimensions, as seen in Figure 4. This type of

Table 3. Average Energies of the First Four States for the One-, Two-, and Three-Dimensional Morse Oscillator Systems[a]

level	exact [E_h] uncoupled	QTAG [E_h] uncoupled	QTAG [E_h] coupled
1D			
0	−0.16619	$-0.16613 \pm 3 \times 10^{-5}$	—
1	−0.14742	-0.1467 ± 0.0005	—
2	−0.12977	-0.126 ± 0.003	—
3	−0.11325	-0.102 ± 0.007	—
2D			
0, 0	−0.33238	$-0.33233 \pm 3 \times 10^{-5}$	$-0.33240 \pm 2 \times 10^{-5}$
1, 0	−0.31361	$-0.31354 \pm 6 \times 10^{-5}$	-0.3162 ± 0.0002
0, 1	−0.31361	-0.3133 ± 0.0004	-0.3108 ± 0.0002
1, 1	−0.29484	-0.2956 ± 0.0003	-0.2998 ± 0.0006
3D			
0, 0, 0	−0.49858	$-0.49853 \pm 2 \times 10^{-5}$	$-0.49873 \pm 4 \times 10^{-5}$
1, 0, 0	−0.47980	$-0.47976 \pm 2 \times 10^{-5}$	$-0.48260 \pm 4 \times 10^{-5}$
0, 1, 0	−0.47980	$-0.47973 \pm 3 \times 10^{-5}$	$-0.48252 \pm 7 \times 10^{-5}$
0, 0, 1	−0.47980	-0.47964 ± 0.0002	$-0.47512 \pm 6 \times 10^{-5}$

[a]The uncertainty terms reflect the standard deviation of each quantity throughout the course of the simulations. The listed exact QM values are the analytic solutions to the uncoupled oscillator problem.

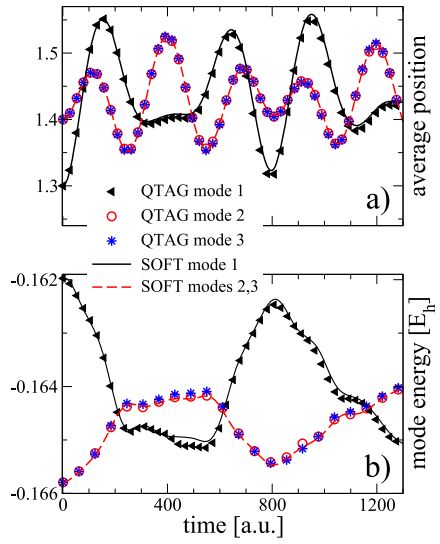

Figure 4. (a) Average positions (au) and (b) mode energies as functions of time for the three coupled Morse oscillators described in Table 1. The legend applies to both panels: "QTAG" labels results obtained using 843 GBFs; "SOFT" labels results for modes 2 and 3, obtained using 262×10^3 equidistant grid points, which are indistinguishable on the graph.

DOI: 10.1021/acs.jctc.9b00844
J. Chem. Theory Comput. 2020, 16, 18−34

behavior is typical in describing molecular vibrations, as a vibration that becomes excited through some external process can dissipate its energy into other appropriately coupled modes. The basis scaling is similar to that of a static basis/grid description of an anharmonic system. As mentioned in Section 4.1, adding a time-dependent basis width improved the overall simulation stability in one dimension; however, because no reexpansions were triggered in the frozen cases, its inclusion would not reduce the number of basis functions needed throughout the propagation. Thus, we have used real frozen GBFs for the two- and three-dimensional calculations.

4.3. Multidimensional Dynamics with Tunneling. In the anharmonic bath model of Section 4.2, the basis size scales essentially as a fixed-grid basis because the wave function remains rather localized in space. The target systems for the time-dependent bases, however, are those exhibiting large-amplitude motion coupled to bath modes representing a molecular environment. Usually, such systems are modeled by one (or a few) challenging mode(s) coupled to multiple harmonic bath modes.

Therefore, the scaling of a quantum dynamics method with system size is typically tested on a condensed-phase model comprised of a double well potential coupled in some fashion to a bath of harmonic oscillators; see, for example, models I and II of refs 55 and 56 and models I–III of ref 50. To gauge the performance of the QTAG approach in this regime, we examine model I of Wu and Batista (referred to as "Wu–Batista" in this work), which consists of a wide double well linearly coupled to a chain of harmonic oscillators (see Table 1). This model has been used to illustrate both classically driven GBF dynamics and the basis expansion leaping approach[24,56,57] for systems containing up to $N = 20$ degrees of freedom.

We find that, within our current QTAG implementation, the bath modes can be represented by two frozen basis functions per dimension, thanks to their coherent wavepacket character. Based on dynamics for $N = 2$, 4, and 6, the basis scaling is $N_b = n_1 2^{N-1}$, where n_1 is the number of basis functions used for the double-well dimension and $N - 1$ the total number of bath modes. We anticipate—and plan to test in the future—that even larger bath sizes can be treated if the GBF positions in the bath modes are updated according to the classical force, which is correct for Gaussian wavepacket dynamics in a quadratic potential.

Figure 5 shows the "reactant/product" correlation functions $C(t) = \langle\psi(-x, 0)|\psi(x, t)\rangle$, computed for the Wu–Batista model with one, three, and five bath modes ($N = 2$, 4, and 6, respectively). The total simulation times of 100 au capture the wave function transfer from the left to the right well in each case. A visual comparison of the top panel of Figure 5 with the bottom panel of Figure 1 in ref 55 shows qualitatively similar frequencies in $\mathcal{R}(C(t))$ and magnitudes in $C(t)$. Figure 5 also shows that the 2D system becomes less stable than its 4D and 6D counterparts as the simulations progress. This trend is typically attributed to the more pronounced quenching of quantum coherences due to energy redistribution across the modes of larger bath models. However, this instability seems to have only a minimal impact on the quality of the computed tunneling correlation function; the microstructure of $|C(t)|$ presented in Figure 5 deviates from exact SOFT values, but the overall tunneling is captured qualitatively. Furthermore, because the 2D system is still relatively small, a calculation using a larger basis in the bath dimension is also feasible. To this end, results using a 17 × 11 grid of basis functions are also presented in Figure 5 and are in better agreement with the exact values, as is expected. These simulations have been performed using the BOT algorithm; their propagation stability is illustrated in Figure 8.

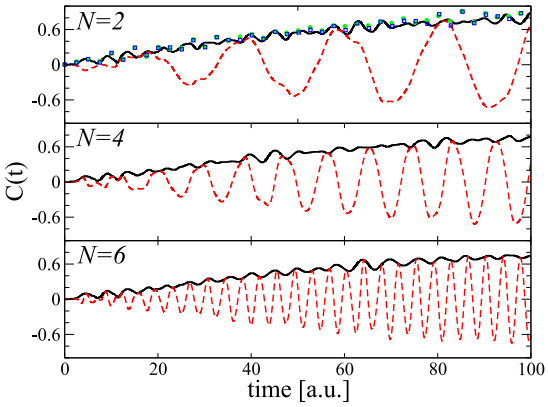

Figure 5. Tunneling correlation functions for the Wu–Batista systems in two (top), four (middle), and six (bottom) dimensions. The solid black lines show the magnitudes $|C(t)|$ of the correlation functions, while the red dashes represent their real components $\mathcal{R}(C(t))$. Also shown for the 2D case are QTAG results using a larger basis ($n_2 = 11$) in the bath dimension (green circles) and exact QM values computed using the SOFT method (blue squares).

4.4. Inversion of Ammonia and Vibrational Mode Dynamics. The inversion mode of ammonia, a vibration in which the three hydrogen atoms undergo a synchronous wagging motion across the nitrogen center, is both well-known and well-studied.[58–60] The source of this phenomenon resides with the quantum nature of the hydrogen nuclei themselves; due to their relatively light masses, they are able to tunnel between the equilibrium C_{3V} geometries, through the energy barrier of about 22.5 kJ/mol corresponding to the planar transition state. The simplest PES describing this motion can be represented by a one-dimensional double-well potential along the tunneling coordinate, which, combined with the coordinate-dependent mass, successfully reproduces both the gap between and splittings of the ground and the first excited state energy levels to within fractions of a wavenumber.[61] This model is thus both chemically relevant and challenging for the trajectory-based dynamics methods, despite its one-dimensional character. We use $V(x)$ represented by a quartic polynomial[62] and compare the QTAG calculations to the conventional time-dependent quantum calculations obtained with the SOFT method[11,63] on an equidistant grid. The energy spectrum is calculated via the Fourier transform of the autocorrelation function $C(t)$, which for an initially real wave function is computed as $C(t) = \langle\psi^*(x, t/2)|\psi(x, t/2)\rangle$. At time $t = 0$, the wave function is taken as a Gaussian wavepacket of eq 55.

The system and wave function parameters are listed in Table 1. At $t = 0$ the wave function is localized in the right-hand-side well, and its energy of 2.88×10^{-3} E_h is about 1/3 of the barrier height, meaning that the classical motion over the barrier top is indeed suppressed. The energy level splitting for the lowest and second lowest pairs of eigenstates are around 3 and 150 microhartree.

The QTAG calculations are performed with real frozen Gaussians, so the only time-dependent parameters of eq 5 are

DOI: 10.1021/acs.jctc.9b00844
J. Chem. Theory Comput. 2020, 16, 18–34

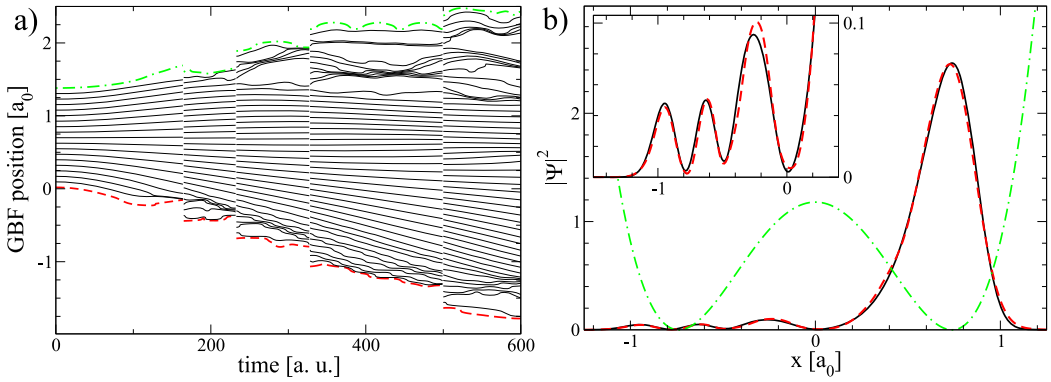

Figure 6. NH_3 inversion model. (a) GBF positions over the course of dynamics beginning with 19 functions. The initial wave function is localized in the right well (positive y values) and tunnels to the left. The dashed and dotted-dashed lines indicate the edge trajectories. (b) Probability density $|\psi|^2$ at t = 2000 au obtained from the fixed-grid/SOFT and QTAG propagations. Zoomed-in view of the left well and barrier regions is shown in the inset. The potential scaled along the vertical axis is shown as the dashed line in panel (b).

the basis positions $\{q_j\}$. As mentioned earlier, this choice trades efficiency in the basis for numerical stability. Multiple simulations were initialized with 15−19 basis functions to represent the starting wave function and propagated for t = 800 au with the time step τ = 1 au. The wave function reexpansions, employing a uniform grid of GBFs, were performed by tracking the quantity $\delta E_j = dE/dq_j$ for the left-most and right-most trajectories, as seen in eq 53. When δE_j for either trajectory exceeded a predefined value f_c, the reexpansion process was initiated. In the case of ammonia tunneling, we prefer tracking the energetics relative to these edge trajectories because they are more sensitive to the wave function time evolution than the total energy alone. The number of reexpansions somewhat varied between simulations, although by t = 600 au the basis size invariably grew to $N_b \approx$ 60 in each case. As evident from the top panel of Figure 6, this increase is necessary for the NH_3 system—particularly when using frozen Gaussians—as the wave function becomes highly dispersed relative to its initial state. The total energy is used to monitor basis completeness and numerical stability during the dynamics and reexpansions; this quantity was conserved within 20 microhartree for the numerical value f_c = 0.001 chosen by trial.

The use of the BOT algorithm seen in Section 3.1 has been essential in generating $C(t)$ of sufficient accuracy and length to resolve the tunneling splittings. The time evolution according to eq 9 using a popular Runge−Kutta integrator used for the QT-guided dynamics previously[47] required a 1000-times smaller time step and, for stability reasons, fewer GBFs. Still, the accuracy of the wave function in the left well was lower; the tunneling splittings could not be resolved, even with the harmonic inversion of the signal, though the ground state energy itself was quite accurate. The energy levels obtained with the new propagator and with SOFT QM calculations, given in Table 4, are in excellent agreement. A comparison of the probability density at the final time t = 2000 au is displayed in Figure 6b: the low amplitude features outside the right well, shown in the inset, are essential to capture tunneling. In this regard, the challenge in the QTAG scheme is to generate trajectory dynamics which takes basis functions across the barrier despite their low initial energy. The propagation with a starting basis consisting of 19 GBFs is quite stable through t = 2000 au, as evidenced by the conservation of total energy to within 1%. By the final time, the basis size increased to 81 GBFs, although we note that for this system the basis could have been kept static past t = 800 au (N_b = 74), when the wave function became delocalized over both wells.

Table 4. Inversion Mode of Ammonia[a]

level	fixed-grid [E_h]	QTAG [E_h]
0^+	2.295×10^{-3}	2.295×10^{-3}
0^-	2.298×10^{-3}	2.297×10^{-3}
1^+	6.348×10^{-3}	6.348×10^{-3}
1^-	6.504×10^{-3}	6.503×10^{-3}

[a]The ground and excited state energies were obtained from the SOFT and QTAG (19 GBFs) methods.

Finally, we have implemented a two-dimensional model where the tunneling coordinate is linearly coupled to a harmonic oscillator with a force constant derived from the frequency of the H−N−H bending motion and an effective mass of approximately twice the reduced mass of NH (see Table 1). The wave function in the oscillator direction is centered in the quadratic well and is essentially coherent. Initially, the density threshold ρ_c for basis placement is taken to be the same as in the 1D simulations; ρ_c is increased by 5 orders of magnitude in the subsequent reexpansions. This prevents an explosion in the number of basis functions used because of the increased dimensionality, while having little impact on the accuracy of the calculation at large. In fact, the initial ρ_c is taken so small in order to have reasonable spacing between the basis functions during reexpansions of the delocalized wave function at later times (the grid-based reexpansion procedure used preserves the initial basis function spacing). Propagation for t = 800 au is achieved with seven grid-based reexpansions occurring at 100 au intervals, and the basis size has changed from 103 to 269 GBFs; the resultant wave function, shown in Figure 7, is in good agreement with the SOFT result.

5. CONCLUSIONS

In this paper we have presented an approach to quantum dynamics built upon the coevolution of a wave function in a basis comprised of time-dependent Gaussian functions and the underlying Bohmian-like trajectories upon which they are placed. Unlike methods based on the variational definition of the GBF parameters or on the classical motion of the GBF centers, we argue that efficient representation of a time-

DOI: 10.1021/acs.jctc.9b00844
J. Chem. Theory Comput. 2020, 16, 18−34

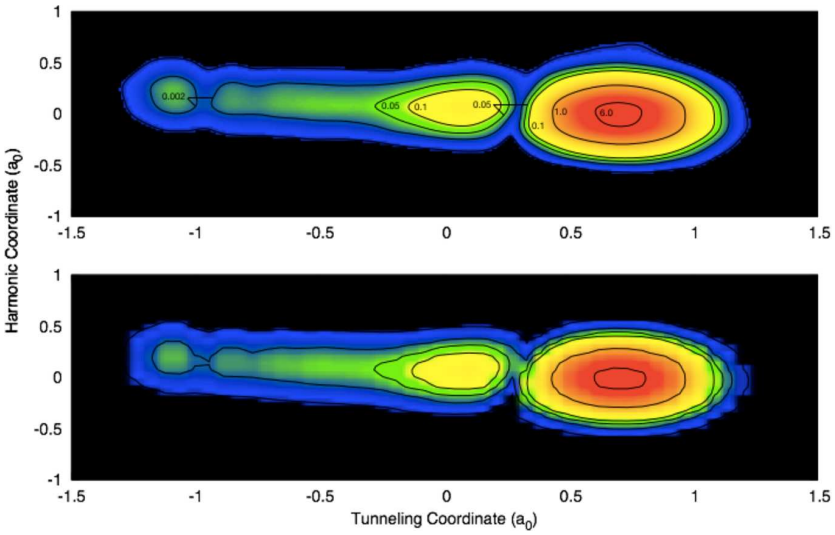

Figure 7. Heat map of the 2D NH_3 system computed for the QTAG (top) and SOFT (bottom) methods. The values shown on the contours in the top panel apply to the bottom panel as well and represent the relevant probability densities; note that they must be scaled nonlinearly to map the full range of $|\psi^2|$ in one image. The underlying color coding is a visual aid to interpolate between the contours and ranges from black ($|\psi^2| = 0.0$) to red ($|\psi^2| = 6.0$). The resolution in the bottom panel is restricted by the number of points used to compute the wave function in the fixed grid method.

dependent wave function is achieved when the GBF dynamics is linked to the conservation of the probability density in coordinate space, which is the central feature of the quantum trajectory formulation of the TDSE.

Indeed, the connection between the wave function and GBFs is apparent by considering the time dependence of the GBF parameters; their positions and widths change according to their momenta and its gradient, respectively, which in turn are determined by the wave function phase. Furthermore, an overall "quantum" phase may also be assigned to each GBF which reduces oscillatory behavior of the basis expansion coefficients and improves stability of the numerical implementation. Altogether, this describes exact quantum dynamics which employs QT-guided Adaptable Gaussian (QTAG) bases. The conceptual advantages of the proposed method are that (i) it does not rely on the variational equations of motion for the GBF parameters, known to be singular in the complete basis limit; (ii) the proposed formulation couples the guiding trajectories through the evolving wave function, which in principle, unlike classical trajectories, reaches all regions of space relevant to quantum processes, including tunneling processes; and (iii) the time-dependent GBF width reduces the basis size required to describe dynamics of dispersing wave functions compared to popular frozen GBF methods. We also note that dynamics is essential to keep the GBF width real, i.e., to limit the GBF phase to be linear in coordinates; this in turn avoids the known problems of thawed GBF dynamics.

The QTAG dynamics shares certain problems with the Gaussian MCTDH and Coupled Coherent Gaussians methods, including the numerical stability issues related to solving the coupled equations of motion for the GBF parameters and expansion coefficients, the expense of evaluation of the potential energy matrix elements, and the sensitivity to sampling of initial wave functions in high dimensionality. Fortunately, the commonality of these problems suggests that the QTAG method can both take advantage of and contribute to the solutions developed in the dynamics community. To alleviate the numerical stability issue, we have developed the basis orthogonalization/transformation (BOT) algorithm, based on the eigenstates of the Hamiltonian expressed in a static nonorthogonal basis paired with transformations describing the basis "adaptation" over time. The latter may include the basis time dependence driven by the QT dynamics, as well as wave function reexpansions to augment or prune the basis according to changes in the underlying probability density. Ultimately, this propagation scheme has been very useful for describing strongly anharmonic motion and tunneling dynamics in a double well; however, traditional integrators are likely to be more efficient in the nearly classical regime of translational motion. We note that the QTAG method could be further tuned by an adaptable time step for more robust basis/wave function coevolution and made more efficient by implementing correlated GBFs for high-dimensional systems. Other applications of the QTAG method we intend to pursue include nonadiabatic and mixed quantum/semiclassical dynamics, which is efficient for chemical processes involving a large-amplitude motion of system fragments coupled to a molecular environment, or even time-dependent external potentials.

APPENDIX A: QUANTUM TRAJECTORY DYNAMICS

The Madelung−de Broglie−Bohm, also referred to as the hydrodynamic or QT formulation of the TDSE,[40,42,64] is based on the polar representation of a complex wave function, expressed in terms of real amplitude $\mathcal{A}(x, t)$ and phase $\mathcal{S}(x, t)$,

$$\psi(x, t) = \mathcal{A}(x, t) \exp\left(\frac{\imath}{\hbar}\mathcal{S}(x, t)\right) \tag{56}$$

Substitution of the ansatz 56 into the TDSE 1 leads to the following time dependence of the wave function phase $\mathcal{S}$ and the probability density ρ:

DOI: 10.1021/acs.jctc.9b00844
J. Chem. Theory Comput. 2020, 16, 18−34

$$\rho(x, t) := |\psi(x, t)|^2 = \mathcal{A}^2 \tag{57}$$

$$\frac{\partial \mathcal{S}}{\partial t} = -\frac{1}{2m}\nabla^2 \mathcal{S} - V - U \tag{58}$$

$$\frac{\partial \rho}{\partial t} = -\frac{\nabla \mathcal{S}}{m}\nabla\rho - \frac{\nabla^2 \mathcal{S}}{m}\rho \tag{59}$$

The time-dependent function $U \equiv U(x, t)$ denotes the *quantum* potential, as opposed to the *classical* potential V,

$$U := -\frac{\hbar^2}{2m}\frac{\nabla^2 \mathcal{A}}{\mathcal{A}} \tag{60}$$

For convenience, we also give an equivalent form of U in terms of the *nonclassical* component of the momentum operator,

$$r(x, t) := \frac{\nabla \mathcal{A}}{\mathcal{A}} \tag{61}$$

$$U := -\frac{\hbar^2}{2m}(r^2 + \nabla r) \tag{62}$$

Equation 62 expresses U in terms of $r(x, t)$, which can be estimated from fitting, interpolation, etc. on par with $p(x, t)$ in numerical implementation schemes.

To highlight the physical meaning of eqs 58 and 59, we define the momentum *function*

$$p(x, t) := \nabla \mathcal{S}(x, t) \tag{63}$$

Evaluated at the trajectory position q_t, the latter gives the *trajectory momentum* p_t,

$$p_t = \nabla \mathcal{S}|_{x=q_t}, \qquad \frac{\mathrm{d}q_t}{\mathrm{d}t} = \frac{p_t}{m} \tag{64}$$

Switching to the Lagrangian frame-of-reference,

$$\frac{\mathrm{d}}{\mathrm{d}t} = \frac{\partial}{\partial t} + \frac{p_t}{m}\nabla \tag{65}$$

one obtains the quantum Hamilton–Jacobi equation for $\mathcal{S}_t$ and the continuity equation for ρ_t *along* the QT:

$$\frac{\mathrm{d}\mathcal{S}_t}{\mathrm{d}t} = \frac{p_t^2}{2m} - (V + U)|_{x=q_t} \tag{66}$$

$$\frac{\mathrm{d}\rho_t}{\mathrm{d}t} = -\frac{\rho_t}{m}\nabla p(x, t)|_{x=q_t} \tag{67}$$

The time evolution equation for the momentum of the trajectory q_t, completing Newton's equations of a QT, is derivable from transforming the gradient of eq 58 into the Lagrangian frame-of-reference according to eq 65,

$$\frac{\mathrm{d}p_t}{\mathrm{d}t} = -\nabla(V + U)|_{x=q_t}$$

As seen from eq 66, in the QT formulation all quantum effects in dynamics of $\psi(x, t)$ come from the quantum potential U given by eq 60. On one hand, $U = U(x, t)$ is, in general, a nonlocal time-dependent function responsible for the exponential scaling of quantum mechanics in the QT formulation of TDSE.[65] On the other hand, U vanishes in the classical limit of infinite mass or $\hbar \to 0$, which suggests that the QT dynamics of the nuclei (which are heavy quantum particles) may be interpreted as classical dynamics with quantum corrections.[66,67]

The efficiency of the QT description of a wave function follows from eq 67, according to which ρ within the volume element δx of each trajectory is conserved,[66]

$$\rho(q_t)\delta q_t = \rho(q_0)\delta q_0 \tag{68}$$

Thus, a single QT ensemble accurately representing $\psi(x, 0)$ will provide an adequate representation of $\psi(x, t)$ at all times. The catch is that the numerical implementation of eq 66 is, in general, impractical: U becomes singular as $\psi(x, t) \to 0$. Another interpretation of exact QTs is that they define a time-dependent grid, self-adjusting for optimal representation of a specific $\psi(x, t)$.

APPENDIX B: QUANTUM HAMILTON–JACOBI EQUATION FOR A QTAG FUNCTION

Substituting a Gaussian $g(x, t)$ of eq 28 with real parameters a_t, q_t, p_t, s_t into the TDSE and dividing by $g(x, t)$ (eq 31) gives a complex equation whose imaginary part results in the following relationship:

$$\dot{q}_t = \frac{\mathcal{S}'(q_t)}{m}, \qquad \dot{a}_t = -\frac{2\mathcal{S}''(q_t)}{m}a_t \tag{69}$$

The real part of eq 31 can be written as

$$U_g(x) + V(x) - \frac{(\mathcal{S}'(q_t))^2}{2m} + \frac{(\mathcal{S}''(q_t)(x - q_t))^2}{2m} + \dot{\mathcal{S}}(q_t) + \dot{\mathcal{S}}'(q_t)(x - q_t) + \frac{\dot{\mathcal{S}}''(q_t)}{2}(x - q_t)^2 = 0 \tag{70}$$

where

$$U_g(x) := -\frac{a_t^2(x - q_t)^2}{2m} + \frac{a_t}{2m} \tag{71}$$

Equation 71 is consistent with the general definition of the quantum potential (eq 60) applied to a Gaussian $g(x, t)$. The $\mathcal{S}$-containing terms in eq 70 can be simplified using the time derivative of the Taylor-expanded $S(x, t)$ (eq 30),

$$\frac{\partial \mathcal{S}(x, t)}{dt} = \dot{\mathcal{S}}(q_t) + \dot{\mathcal{S}}'(q_t)(x - q_t) + \frac{\dot{\mathcal{S}}''(q_t)}{2}(x - q_t)^2 - \dot{q}_t\nabla \mathcal{S}(x, t) \tag{72}$$

where

$$\dot{q}_t\nabla \mathcal{S}(x, t) = \frac{\mathcal{S}'(q_t)}{m}(\mathcal{S}'(q_t) + \mathcal{S}''(q_t)(x - q_t)) \tag{73}$$

Using eqs 72 and 73 and switching to the Lagrangian frame-of-reference, $\mathrm{d}/\mathrm{d}t = \partial/\partial t + \dot{q}_t\nabla$, eq 70 becomes

$$U_g(x) + V(x) + \frac{\partial \mathcal{S}}{\partial t} + \frac{(\mathcal{S}'(q_t) + \mathcal{S}''(q_t)(x - q_t))^2}{2m} = U_g(x) + V(x) + \frac{\mathrm{d}\mathcal{S}}{\mathrm{d}t} - \frac{(\nabla \mathcal{S})^2}{2m} = 0 \tag{74}$$

Expression 74 is equivalent to the quantum Hamilton–Jacobi equation,

$$\frac{\mathrm{d}\mathcal{S}(q_t)}{\mathrm{d}t} = \frac{p_t^2}{2m} - (U + V)|_{x=q_t} \tag{75}$$

DOI: 10.1021/acs.jctc.9b00844
J. Chem. Theory Comput. 2020, 16, 18–34

Table 5. Wavefunction Propagation Procedure with Basis Transformations[a]

	operation	input	output
start	solve $\mathbf{HZ} = \mathbf{SZ}\mathcal{E}$	$\mathbf{H}$, $\mathbf{S}$, t	diagonal $\mathcal{E}$, $\mathbf{Z}$, $\mathbf{S}^{-1} = \mathbf{Z}\cdot\mathbf{Z}^{\dagger}$
(i)	propagate by τ	$\vec{b}$, $\vec{c}$	$\vec{c}(t+\tau) = \mathbf{Z}e^{-\imath\mathcal{E}\tau}\mathbf{Z}^{\dagger}\vec{b}(t)$, $\vec{b}(t) = \mathbf{S}\vec{c}(t)$
(ii)	define new basis	$\vec{g}_{old}$	$\vec{g}_{new}$, $\mathbf{H}_{new}$, $\mathbf{S}_{new}$
(iii)	solve $\mathbf{HZ} = \mathbf{SZ}\mathcal{E}$	$\mathbf{H}_{new}$, $\mathbf{S}_{new}$	new $\mathcal{E}$, $\mathbf{Z}$, $\mathbf{S}_{new}^{-1}$
(iv)	transform to $\vec{g}_{new}$	$\vec{b}$, $\vec{c}$, $\vec{g}_{new}$, $\vec{g}_{old}$	$\vec{b}_{new} = \mathbf{T}\vec{c}_{old}$, $\vec{c}_{new}=\mathbf{S}_{new}^{-1}\vec{b}_{new}$
(v)	"observables"	$\vec{c}$, $\vec{g}$, $\mathbf{H}$, $\mathbf{S}$	$\psi(x,t)$, $\langle\psi\hat{H}\psi\rangle = \vec{c}^{\dagger}\mathbf{H}\vec{c}$ etc.
(vi)	relabel *new* as *old* and $t+\tau$ as t		continue to (i) or **stop**

[a]Definitions: $\psi(x,t) = \sum_{i=1}^{N_b} c_i(t)g_i(x)$, $\vec{b} = \langle\vec{g}|\psi\rangle$, $\vec{c} = \mathbf{S}^{-1}\vec{b}$, where $\mathbf{S} = \langle\vec{g}\otimes\vec{g}\rangle$. The basis transformation matrix $\mathbf{T} = \langle\vec{g}_{new}\otimes\vec{g}_{old}\rangle$. The time increment τ does not need to be small, as long as $\vec{g}$ adequately represents ψ throughout τ.

once the trajectory momentum is identified as the QT momentum (eq 63), as

$$p_t = \nabla\mathcal{S}|_{x=q_t} = \mathcal{S}'(q_t) \tag{76}$$

Equation 75 defines the time evolution of the wave function phase along the quantum (or Bohmian) trajectory $\{q_t, p_t\}$, evolving according to

$$\dot{q}_t = \frac{p_t}{m}, \quad \dot{p}_t = -\nabla(U+V)|_{x=q_t} \tag{77}$$

Therefore, we argue that the locally variational GBF parameters are defined by the dynamics of the QT attributes summarized by eq 39.

APPENDIX C: PROPAGATOR FOR THE NONORTHOGONAL BASIS

The wave function propagator in a static nonorthogonal basis (eqs 3 and 4), is constructed from solutions to the generalized eigenvalue problem

$$\mathbf{HZ} = \mathbf{SZ}\mathcal{E} \tag{78}$$

The elements of the Hamiltonian $\mathbf{H}$ and of the overlap matrix $\mathbf{S}$ are given by eqs 11 and 10, respectively. The diagonal matrix $\mathcal{E}$ contains the energy eigenvalues, $\mathcal{E}_{jj} = \varepsilon_j$, while the columns of the matrix $\mathbf{Z}$ give the Hamiltonian eigenvectors in a basis $\vec{g}$. The eigenvectors satisfy the following relationships:

$$\mathbf{Z}^{\dagger}\mathbf{SZ} = \mathbf{I}, \quad \mathbf{ZZ}^{\dagger} = \mathbf{S}^{-1} \tag{79}$$

Propagation within the static basis $\vec{g}$ by t updates the expansion coefficients as

$$\vec{c}(t) = \mathbf{U}_t\vec{c}(0) \tag{80}$$

where the matrix

$$\mathbf{U}_t := \mathbf{Z}e^{-\imath\mathcal{E}t}\mathbf{Z}^{\dagger}\mathbf{S} \tag{81}$$

is the *nonorthogonal basis* propagator. Using properties 79, propagation over t_1 followed by propagation over t_2 is

$$\mathbf{U}_{t_2}\mathbf{U}_{t_1} = \mathbf{Z}e^{-\imath\mathcal{E}t_2}\underbrace{\mathbf{Z}^{\dagger}\mathbf{SZ}}_{\mathbf{I}}e^{-\imath\mathcal{E}t_1}\mathbf{Z}^{\dagger}\mathbf{S} = \mathbf{Z}e^{-\imath\mathcal{E}(t_2+t_1)}\mathbf{Z}^{\dagger} = \mathbf{U}_{t_1+t_2} \tag{82}$$

A forward/backward propagation over t is a unit matrix,

$$\mathbf{U}_{-t}\mathbf{U}_t = \mathbf{Z}e^{\imath\mathcal{E}t}\underbrace{\mathbf{Z}^{\dagger}\mathbf{SZ}}_{\mathbf{I}}e^{-\imath\mathcal{E}t}\mathbf{Z}^{\dagger}\mathbf{S} = \underbrace{\mathbf{ZZ}^{\dagger}}_{\mathbf{S}^{-1}}\mathbf{S} = \mathbf{I} \tag{83}$$

Notice that the Hamiltonian is assumed to be unchanging across the interval $t_1 + t_2$.

Using superscripts to label distinct bases, the basis transformation from $\vec{g}^{(k-1)}$ to $\vec{g}^{(k)}$ is described by the matrix,

$$T_{jl}^{(k,k-1)} = \langle g_j^{(k)}|g_l^{(k-1)}\rangle \tag{84}$$

The expansion coefficients are transformed accordingly:

$$\vec{c}^{(k)} = (\mathbf{S}^{(k)})^{-1}\mathbf{T}^{(k,k-1)}\vec{c}^{(k-1)} \tag{85}$$

Combined with the time propagation by τ,

$$\begin{aligned}\vec{c}^{(k)}(t+\tau) &= \mathbf{U}_{\tau}^{(k)}\vec{c}^{(k)}(t)\\ &= \underbrace{\mathbf{Z}^{(k)}e^{-\imath\mathcal{E}^{(k)}\tau}\mathbf{Z}^{(k)\dagger}}_{\mathbf{K}_{\tau}^{(k)}}\mathbf{T}^{(k,k-1)}\vec{c}^{(k-1)}(t)\end{aligned} \tag{86}$$

from which eq 48 follows. The matrix $\mathbf{K}_{\tau}^{(k)}$ is the propagator of eq 45 in Section 3.1. The steps of the propagation algorithm are summarized in Tables 5 and 6.

Table 6. Basis Propagation Procedure as a Supplement to Entry (ii) of Table 5[a]

	operation	input	output	eq
(a)	calculate trajectory momentum	$\vec{c}(t+\tau)$, $\vec{\lambda}(t)$	$z \approx \nabla\psi/\psi$	38
(b)	update positions	$q(t)$,$\dot{q} = \mathcal{I}(z)/m$	$q(t+\tau)$	37
(c)	update widths	$a(t)$, $\dot{a} = -2\nabla(\mathcal{I}(z))/m$	$a(t+\tau)$	37
(d)	update overall phases	$s(t)$, $V(q)$, $\mathcal{R}(z)$, $\nabla(\mathcal{R}(z))$	$s(t+\tau)$	37, 62
(e)	define linear phases	z	$p(t+\tau) := \mathcal{I}(z)$	39

[a]The sets of parameters $\vec{\lambda}(t)$ and $\vec{\lambda}(t+\tau)$ correspond to the bases $\vec{g}_{old}$ and $\vec{g}_{new}$, respectively. The log-derivative z is a smoothed "fit" to $\nabla\psi/\psi$, ψ computed in a basis. The linear GBF phase is equal to $p(x-q)$. Entries (b–e) may be performed in any order.

Note that this style of propagation is equivalent to trajectory dynamics with a standard integrator in the limit of increasingly frequent projections; this equivalence, coupled with the statements contained in the concluding paragraph of Section 3.2, indicates that the degree of basis overlap throughout a QTAG simulation is a two-component issue related to both the time step taken between projections and the quality of the trajectories themselves. To this end, we monitor the normalization of the wave functions used across multiple simulations in various dimensionalities and find that—for the model problems presented—the QT character of the trajectories is sufficient to preserve basis overlap even with increasing dimensionality (see the top panel of Figure 8). The degree to which the normalization decays is instead largely a function

DOI: 10.1021/acs.jctc.9b00844
J. Chem. Theory Comput. 2020, 16, 18–34

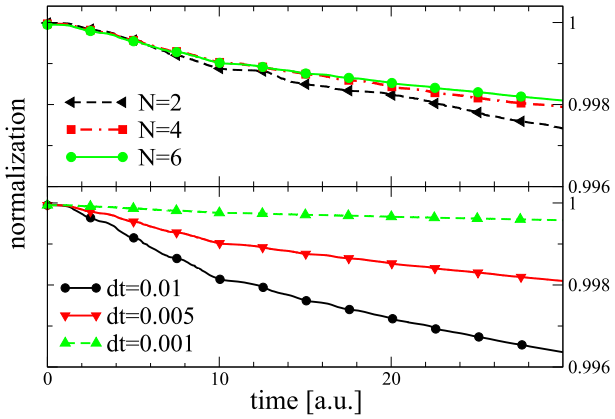

Figure 8. Normalization conservation as a function of the first 30 au of simulation time for the high-dimensionality Wu−Batista model 1 systems. The black line with filled circles is the same across both panels. Top: Normalization as a function of increasing number of degrees of freedom. The rationale for the somewhat poor conservation in the 2D case is discussed in the text (Section 4.3). Bottom: Normalization as a function of time step for the largest-dimensionality system.

of the time step taken between projections, as demonstrated in the bottom panel of Figure 8. Thus, the remedy for the decaying basis overlap is, in the systems presented here, the same as for the standard dynamics case.

APPENDIX D: MULTIDIMENSIONAL GENERALIZATION OF QTAG DYNAMICS

In d Cartesian dimensions the mass becomes a diagonal matrix $\mathbf{M}$, the coordinates are given by a vector $\vec{x}$, and $\vec{\nabla}$ denotes a vector. The GBF function is

$$g_j(\vec{x};\lambda_j(t)) = \frac{\pi^{d/4}}{(\det \mathbf{A})^{1/4}} \exp\left(-\frac{1}{2}(\vec{x}-\vec{q}_j)^T\mathbf{A}_j(\vec{x}-\vec{q}_j) + \imath\vec{p}_j^T(\vec{x}-\vec{q}_j) + \imath s_j\right) \tag{87}$$

The center and linear phase parameters for each jth GBF generalize to vectors $\vec{q}_j$ and $\vec{p}_j$ and are updated/assigned as

$$\frac{d\vec{q}_j}{dt} = \mathbf{M}^{-1}\mathcal{I}(\vec{z}_j), \quad \dot{\vec{p}}_j = \mathcal{I}(\vec{z}_j), \quad \vec{z}_j \approx \psi^{-1}\vec{\nabla}\psi|_{\vec{x}=\vec{q}_j} \tag{88}$$

The width a_j becomes a real symmetric matrix $\mathbf{A}_j$:

$$\frac{d\mathbf{A}_j}{dt} = -2\vec{\nabla}\otimes(\mathbf{M}^{-1}\vec{z}_j)\mathbf{A}_j \tag{89}$$

where $\otimes$ denotes the tensor product. The GBF phase s_j evolves according to

$$\frac{ds_j}{dt} = \frac{1}{2}\vec{p}_j^T\mathbf{M}^{-1}\vec{p}_j - V(q_j) - U_j \tag{90}$$

where U_j is the quantum contribution,

$$U_j = -\frac{1}{2}(\vec{r}_j^T\mathbf{M}^{-1}\vec{r}_j + \vec{\nabla}^T\mathbf{M}^{-1}\vec{r}_j), \quad \vec{r}_j \approx \vec{\nabla}(\ln|\psi|)|_{\vec{x}=\vec{q}_j} \tag{91}$$

The basis expansion coefficients of ψ evolve according to eq 9 with the integrals in all matrix elements evaluated over the full coordinate space.

AUTHOR INFORMATION

Corresponding Author

*(S.G.) E-mail: garashchuk@sc.edu.

ORCID

Sophya Garashchuk: 0000-0003-2452-7379

Funding

This material is based upon work supported in part by the National Science Foundation and SC EPSCoR/IDeA Program under Grant Nos. CHE-1056185 and OIA-1655740/13020-GA27.

Notes

The authors declare no competing financial interest.

REFERENCES

(1) Shao, M.; Keum, J.; Chen, J.; He, Y.; Chen, W.; Browning, J. F.; Jakowski, J.; Sumpter, B. G.; Ivanov, I. N.; Ma, Y.-Z.; Rouleau, C. M.; Smith, S. C.; Geohegan, D. B.; Hong, K.; Xiao, K. The isotopic effects of deuteration on optoelectronic properties of conducting polymers. *Nat. Commun.* **2014**, *5*, 3180.

(2) Lozada-Hidalgo, M.; Hu, S.; Marshall, O.; Mishchenko, A.; Grigorenko, A. N.; Dryfe, R. A. W.; Radha, B.; Grigorieva, I. V.; Geim, A. K. Sieving hydrogen isotopes through two-dimensional crystals. *Science* **2016**, *351*, 68−70.

(3) Ekanayake, N. T.; Huang, J.; Jakowski, J.; Sumpter, B. G.; Garashchuk, S. Relevance of the Nuclear Quantum Effects on the Proton/Deuteron Transmission through Hexagonal Boron Nitride and Graphene Monolayers. *J. Phys. Chem. C* **2017**, *121*, 24335−24344.

(4) Cai, W.; Dunuwille, M.; He, J.; Taylor, T. V.; Hinton, J. K.; MacLean, M. C.; Molaison, J. J.; dos Santos, A. M.; Sinogeikin, S.; Deemyad, S. Deuterium Isotope Effects in Polymerization of Benzene under Pressure. *J. Phys. Chem. Lett.* **2017**, *8*, 1856−1864.

(5) Nguyen, T. D.; Basel, T. P.; Pu, Y. J.; Li, X.-G.; Ehrenfreund, E.; Vardeny, Z. V. Isotope effect in the spin response of aluminum tris(8-hydroxyquinoline) based devices. *Phys. Rev. B: Condens. Matter Mater. Phys.* **2012**, *85*, 245437.

(6) Rassolov, V. A.; Garashchuk, S. Computational complexity in quantum chemistry. *Chem. Phys. Lett.* **2008**, *464*, 262−264.

(7) Kosloff, D.; Kosloff, R. A Fouirier method solution for the time-dependent Schrodinger equation as a tool in molecular dynamics. *J. Comput. Phys.* **1983**, *52*, 35−53.

(8) Leforestier, C.; Bisseling, R.; Cerjan, C.; Feit, M.; Friesner, R.; Guldberg, A.; Hammerich, A.; Jolicard, G.; Karrlein, W.; Meyer, H.; Lipkin, N.; Roncero, O.; Kosloff, R. A Comparison of different popagation schemes for the time-dependent Schrodinger equation. *J. Comput. Phys.* **1991**, *94*, 59−80.

(9) Kosloff, R. The Fourier Method. *Numerical gird methods and their applications to Schrodinger equation*; Springer: 1993; pp 175−194; NATO Advanced Research Workshop on Grid Methods in Atomic and Molecular Quantum Calculations, Corte, France, Sep. 27−Oct. 03, 1992.

(10) Kosloff, R. Propagation methods for quantum molecular dynamics. *Annu. Rev. Phys. Chem.* **1994**, *45*, 145−178.

(11) Billeter, S.; VanGunsteren, W. A comparison of different numerical propagation schemes for solving the time-dependent Schrodinger equation in the position representation in one dimension for mixed quantum- and molecular dynamics simulations. *Mol. Simul.* **1995**, *15*, 301−322.

(12) Light, J. C.; Carrington, T., Jr. Discrete variable representations and their utilization. *Adv. Chem. Phys.* **2007**, *114*, 263−310.

DOI: 10.1021/acs.jctc.9b00844
J. Chem. Theory Comput. 2020, 16, 18−34

(13) Meyer, H. D.; Manthe, U.; Cederbaum, L. S. The multi-configurational time-dependent Hartree approach. *Chem. Phys. Lett.* **1990**, *165*, 73−78.
(14) Burghardt, I.; Meyer, H.-D.; Cederbaum, L. S. Approaches to the approximate treatment of complex molecular systems by the multiconfiguration time-dependent Hartree method. *J. Chem. Phys.* **1999**, *111*, 2927−2939.
(15) Meyer, H. D.; Worth, G. A. Quantum molecular dynamics: propagating wavepackets and density operators using the multi-configuration time-dependent Hartree method. *Theor. Chem. Acc.* **2003**, *109*, 251−267.
(16) Burghardt, I.; Nest, M.; Worth, G. A. Multiconfigurational system-bath dynamics using Gaussian wave packets: Energy relaxation and decoherence induced by a finite-dimensional bath. *J. Chem. Phys.* **2003**, *119*, 5364−5378.
(17) Roemer, S.; Ruckenbauer, M.; Burghardt, I. Gaussian-based multiconfiguration time-dependent Hartree: A two-layer approach. I. Theory. *J. Chem. Phys.* **2013**, *138*, 064106.
(18) Roemer, S.; Burghardt, I. Towards a variational formulation of mixed quantum-classical molecular dynamics. *Mol. Phys.* **2013**, *111*, 3618−3624.
(19) Jackle, A.; Meyer, H. Product representation of potential energy surfaces. *J. Chem. Phys.* **1996**, *104*, 7974−7984.
(20) Jackle, A.; Meyer, H. Product representation of potential energy surfaces. II. *J. Chem. Phys.* **1998**, *109*, 3772−3779.
(21) Dawes, R.; Passalacqua, A.; Wagner, A. F.; Sewell, T. D.; Minkoff, M.; Thompson, D. L. Interpolating moving least-squares methods for fitting potential energy surfaces: Using classical trajectories to explore configuration space. *J. Chem. Phys.* **2009**, *130*, 144107.
(22) Richings, G. W.; Habershon, S. Direct Quantum Dynamics Using Grid-Based Wave Function Propagation and Machine-Learned Potential Energy Surfaces. *J. Chem. Theory Comput.* **2017**, *13*, 4012.
(23) Richings, G. W.; Worth, G. A. A practical diabatisation scheme for use with the direct-dynamics variational Multi-Configuration Gaussian method. *J. Phys. Chem. A* **2015**, *119*, 12457−12470.
(24) Richings, G. W.; Habershon, S. MCTDH on-the-fly: Efficsient grid-based quantum dynamics without pre-computed potential energy surfaces. *J. Chem. Phys.* **2018**, *148*, 134116.
(25) Habershon, S. Linear dependence and energy conservation in Gaussian wavepacket basis sets. *J. Chem. Phys.* **2012**, *136*, 014109.
(26) Worth, G. A.; Burghardt, I. Full quantum mechanical molecular dynamics using Gaussian wavepackets. *Chem. Phys. Lett.* **2003**, *368*, 502.
(27) Worth, G. A.; Robb, M. A.; Burghardt, I. A novel algorithm for non-adiabatic direct dynamics using variational Gaussian wavepackets. *Faraday Discuss.* **2004**, *127*, 307.
(28) Burghardt, I.; Giri, K.; Worth, G. A. Multimode quantum dynamics using Gaussian wavepackets: The Gaussian-based multi-configuration time-dependent Hartree (G-MCTDH) method applied to the absorption spectrum of pyrazine. *J. Chem. Phys.* **2008**, *129*, 174104.
(29) Shalashilin, D. V.; Burghardt, I. Gaussian-based techniques for quantum propagation from the time-dependent variational principle: Formulation in terms of trajectories of coupled classical and quantum variables. *J. Chem. Phys.* **2008**, *129*, 084104.
(30) Richings, G.; Polyak, I.; Spinlove, K.; Worth, G.; Burghardt, I.; Lasorne, B. Quantum dynamics simulations using Gaussian wavepackets: the vMCG method. *Int. Rev. Phys. Chem.* **2015**, *34*, 269−308.
(31) Ben-Nun, M.; Martínez, T. J. A multiple spawning approach to tunneling dynamics. *J. Chem. Phys.* **2000**, *112*, 6113−6121.
(32) Ben-Nun, M.; Quenneville, J.; Martinez, T. J. Ab initio multiple spawning: Photochemistry from first principles quantum molecular dynamics. *J. Phys. Chem. A* **2000**, *104*, 5161−5175.
(33) Toniolo, A.; Ciminelli, C.; Persico, M.; Martínez, T. J. Simulation of the photodynamics of azobenzene on its first excited state: Comparison of full multiple spawning and surface hopping treatments. *J. Chem. Phys.* **2005**, *123*, 234308.
(34) Levine, B. G.; Coe, J. D.; Virshup, A. M.; Martinez, T. J. Implementation of ab initio multiple spawning in the Molpro quantum chemistry package. *Chem. Phys.* **2008**, *347*, 3−16.
(35) Olsen, S.; Lamothe, K.; Martinez, T. J. Protonic Gating of Excited-State Twisting and Charge Localization in GFP Chromophores: A Mechanistic Hypothesis for Reversible Photoswitching. *J. Am. Chem. Soc.* **2010**, *132*, 1192.
(36) Shalashilin, D. V.; Child, M. S. Real time quantum propagation on a Monte Carlo trajectory guided grids of coupled coherent states: 26D simulation of pyrazine absorption spectrum. *J. Chem. Phys.* **2004**, *121*, 3563−3568.
(37) Shalashilin, D. V. Nonadiabatic dynamics with the help of multiconfigurational Ehrenfest method: Improved theory and fully quantum 24D simulation of pyrazine. *J. Chem. Phys.* **2010**, *132*, 244111.
(38) Makhov, D. V.; Glover, W. J.; Martinez, T. J.; Shalashilin, D. V. Ab initio multiple cloning algorithm for quantum nonadiabatic molecular dynamics. *J. Chem. Phys.* **2014**, *141*, 054110.
(39) Ronto, M.; Shalashilin, D. V. Numerical Implementation and Test of the Modified Variational Multiconfigurational Gaussian Method for High-Dimensional Quantum Dynamics. *J. Phys. Chem. A* **2013**, *117*, 6948−6959.
(40) Madelung, E. Quantum theory in hydrodynamic form. *Eur. Phys. J. A* **1927**, *40*, 322−326.
(41) de Broglie, L. Interference and Corpuscular Light. *Nature* **1926**, *118*, 441−442.
(42) Bohm, D. A suggested interpretation of the quantum theory in terms of "hidden" variables, I and II. *Phys. Rev.* **1952**, *85*, 166−193.
(43) Heller, E. J. Time-dependent approach to semiclassical dynamics. *J. Chem. Phys.* **1975**, *62*, 1544.
(44) Tannor, D. J. *Introduction to Quantum Mechanics: A Time-Dependent Perspective*; University Science Books: 2006.
(45) Kay, K. G. Integral expressions for the semiclassical time-dependent propagator. *J. Chem. Phys.* **1994**, *100*, 4377−4392.
(46) Heller, E. J. Frozen Gaussians: A very simple semiclassical approximation. *J. Chem. Phys.* **1981**, *75*, 2923.
(47) Gu, B.; Garashchuk, S. Quantum Dynamics with Gaussian Bases Defined by the Quantum Trajectories. *J. Phys. Chem. A* **2016**, *120*, 3023−3031.
(48) Wu, Y. H.; Batista, V. S. Matching-pursuit for simulations of quantum processes. *J. Chem. Phys.* **2003**, *118*, 6720−6724.
(49) Koch, W.; Frankcombe, T. J. Basis Expansion Leaping: A New Method to Solve the Time-Dependent Schrodinger Equation for Molecular Quantum Dynamics. *Phys. Rev. Lett.* **2013**, *110*, 263202.
(50) Saller, M. A. C.; Habershon, S. Quantum Dynamics with Short-Time Trajectories and Minimal Adaptive Basis Sets. *J. Chem. Theory Comput.* **2017**, *13*, 3085−3096.
(51) Pettey, L. R.; Wyatt, R. E. Quantum wave packet dynamics on multidimensional adaptive grids: Applications of the moving boundary truncation method. *Int. J. Quantum Chem.* **2007**, *107*, 1566−1573.
(52) Shalashilin, D. V.; Child, M. S. Basis set sampling in the method of coupled coherent states: Coherent state swarms, trains, and pancakes. *J. Chem. Phys.* **2008**, *128*, 054102.
(53) Flynn, S.; Mandelshtam, V. A. Sampling general distributions with quasi-regular grids: Application to the vibrational spectra calculations. Personal communication, 2019.
(54) Garashchuk, S.; Light, J. C. Quasirandom distributed Gaussian bases for bound problems. *J. Chem. Phys.* **2001**, *114*, 3929−3939.
(55) Wu, Y.; Batista, V. S. Quantum tunneling dynamics in multidimensional systems: A matching-pursuit description. *J. Chem. Phys.* **2004**, *121*, 1676−1680.
(56) Sherratt, P. A.; Shalashillin, D. V.; Child, M. S. Description of multidimensional tunnelling with the help of coupled coherent states guided by classical Hamiltonians with quantum corrections. *Chem. Phys.* **2006**, *322*, 127−134.
(57) Murakami, T.; Frankcombe, T. J. Accurate quantum molecular dynamics for multidimensional systems by the basis expansion leaping

DOI: 10.1021/acs.jctc.9b00844
J. Chem. Theory Comput. 2020, 16, 18−34

multi-configuration Gaussian (BEL MCG) method. *J. Chem. Phys.* **2018**, *149*, 134113.
(58) Förster, J.; Saenz, A. Theoretical Study of the Inversion Motion of the Ammonia Cation with Subfemtosecond Resolution for High-Harmonic Spectroscopy. *ChemPhysChem* **2013**, *14*, 1438−1444.
(59) Förster, J.; Plésiat, E.; Magaña, A.; Saenz, A. Imaging of the umbrella motion and tunneling in ammonia molecules by strong-field ionization. *Phys. Rev. A: At., Mol., Opt. Phys.* **2016**, *94*, 043405.
(60) Baiardi, A.; Bloino, J.; Barone, V. Simulation of Vibronic Spectra of Flexible Systems: Hybrid DVR-Harmonic Approaches. *J. Chem. Theory Comput.* **2017**, *13*, 2804−2822.
(61) Aquino, N.; Campoy, G.; Yee-Madeira, H. The inversion potential for NH3 using a DFT approach. *Chem. Phys. Lett.* **1998**, *296*, 111−116.
(62) Ekanayake, N. T.; Garashchuk, S. Evaluation of the quantum time-correlation functions employing the Hamilton−Jacobi dynamics framework. *Theor. Chem. Acc.* **2019**, *138*, 8.
(63) Feit, M. D.; Fleck, J. A., Jr.; Steiger, A. Solution of the Schrödinger equation by a spectral method. *J. Comput. Phys.* **1982**, *47*, 412−433.
(64) de Broglie, L. *An introduction to the study ot wave mechanics*; E. P. Dutton and Company, Inc.: New York, 1930.
(65) Garashchuk, S.; Rassolov, V. A. Stable long-time semiclassical description of zero-point energy in high-dimensional molecular systems. *J. Chem. Phys.* **2008**, *129*, 024109.
(66) Garashchuk, S.; Rassolov, V. A. Energy conserving approximations to the quantum potential: Dynamics with linearized quantum force. *J. Chem. Phys.* **2004**, *120*, 1181−1190.
(67) Garashchuk, S.; Rassolov, V.; Prezhdo, O. Semiclassical Bohmian dynamics. *Reviews in Computational Chemistry*; Wiley: 2011; Vol. *27*, pp 111−210.

DOI: 10.1021/acs.jctc.9b00844
J. Chem. Theory Comput. 2020, 16, 18−34